ABSTRACT

TIME-GATED DIFFUSE OPTICAL SPECTROSCOPY:
EXPERIMENTS ON LAYERED MEDIA

Carter Benjamin McMaster

Propagation of near-infrared light through tissues is characterized by scattering (μ'_s) and absorption (μ_a). Using diffuse optical spectroscopy measurements, μ'_s and μ_a can be quantified and concentrations of absorbing molecules can then be estimated in real time. Time-gated detection has been proven to increase contrast at deeper levels of scattering media; however, the media were assumed to be homogeneous and not layered in past studies. The initial aim of this study was towards resolving deeper optical properties with time-gated detection and layered light propagation models. Characterization of deeper medium layers would certainly lead to implementation of such techniques for monitoring tissue oxygenation underneath the skin and even the skull layers. It was shown that changes in the depth of a sample's superficial layer can be sensed past 15 mm with gated detection whereas in the absence of gating there was no sensitivity. Layered, diffusion-based light propagation model did not accurately predict expected optical properties of the samples measured using time-gated detection. Determining the sources of error that prevented layered modeling of time-gated measurements became the specific objective of the research. Achieving the objective could show whether the layered diffusion model used here is practical for real tissue studies.

TIME-GATED DIFFUSE OPTICAL SPECTROSCOPY:
EXPERIMENTS ON LAYERED MEDIA

A Thesis

Submitted to the
Faculty of Miami University
in partial fulfillment of
the requirements for the degree of
Master of Science
Department of Physics
by
Carter McMaster
Miami University
Oxford, Ohio
2022

Advisor: Karthik Vishwanath

Reader: Paul Urayama

Reader: Samir Bali

This thesis titled

TIME-GATED DIFFUSE OPTICAL SPECTROSCOPY:
EXPERIMENTS ON LAYERED MEDIA

by

Carter Benjamin McMaster

has been approved for publication by

The College of Arts and Sciences
and
Department of Physics

of Miami University

Advisor: _____

(Karthik Vishwanath)

Reader: _____

(Paul Urayama)

Reader: _____

(Samir Bali)

Contents

List of Figures

List of Tables

DEDICATION

This thesis is dedicated to Cherilyn McMaster. From a young age, I valued science because of her clear perspective that is guided by evidence yet never afraid to change.

ACKNOWLEDGEMENTS

I owe my thanks to many people from my family, my lab members, faculty and classmates. In particular I needed help intellectually and emotionally to finish this thesis. For the times when I ran out of inspiration or started to get out of bounds with my ideas, my advisor Dr. Vishwanath helped steer me back in the right direction and give me next steps. For the more than a few times when I was emotionally exhausted and doubt crept in, there was none other than my wife Kitty who I could connect with no matter how down I felt.

Introduction

The research problems investigated here all have to do with optical spectroscopy of highly scattering media. Optics and spectroscopy have vast applications ranging from medical imaging to chemical sensing in outer space. Often, the effect of multiple scattering is avoided in such applications because it makes media appear opaque, milky or turbid.

Research in diffuse optical spectroscopy (DOS) deals with the multiple scattering of near-infrared (NIR) light in tissues. Curiously, a light transport model that was originally developed for use in atmospheric physics and spectroscopy turned out to be the right tool for this task [1]. So why apply light scattering theory to biomedical optics and study tissues with NIR or visible light? Well, because light at these wavelengths interact with compounds that absorb light (chromophores), yielding compositional information that would be "unseen" by say X-ray radiation or ultrasound, or other common imaging techniques used in biomedicine. DOS is about recovering the information contained in the absorption profiles of chromophores despite the high level of scattering.

For over 20 years, DOS has been used in medical and research settings to characterize tissues and monitor blood oxygenation [2, 3, 4, 5, 6]. Light propagation in turbid media is governed by the scattering and absorption properties of the medium–which are quantified using the absorption (μ_a) and reduced scattering (μ_s') coefficients [7]. Optical properties are estimated using the appropriate light propagation model and iteratively fitting the theoretical predictions with the measured data [8]. The light propagation model that physically accounts for scattering is called the radiative transfer equation (RTE) [1].

Diffusion theory (DT) is an approximate way to solve the RTE that is computationally efficient due to the availability of analytical solutions [1]. In diffusion theory, it is usually assumed that the experimental sample is an infinite medium of homogeneous optical properties [9]. This assumption is physically inaccurate because biological media are in fact layered and finite. Further, the superficial layers–skin and subcutaneous fat tissues–contaminate the recovered optical properties when a deeper section of tissue is being investigated, such as the cerebrum or muscle [10].

1

DOS measurements are usually obtained using continuous-wave diffuse reflectance spectroscopy (CWDRS). In CWDRS, a continuous intensity light source is used to illuminate the sample medium directly at the surface. Diffusely reflected light (reflectance) is harvested using an optical fiber in direct contact with the surface at some radial distance, ρ, away from the light source. The resulting intensity of detected light is a function of wavelength and source-detector separation (SDS), the distance between source and detector channel fibers [4, 11]. Although instrumentation for CWDRS is easy to use and inexpensive to obtain, reconstructions of CWDRS measurements are only robust for quantifying relative changes in optical properties rather than determining their absolute values [12]. Further, optical property reconstructions using CWDRS data require knowledge about the spectral absorption profiles of the chromophores [13, 12].

Another form of DOS called time-resolved diffuse reflectance spectroscopy (TRDRS) contains richer information, with the potential to quantify absolute optical properties using a single measurement [14]. for example, TRDRS can be used to resolve absorption change at different depths of the tissue using the statistical moments of photon arrival times [15, 10] or breaking up the integrated signal into time gates [16, 17] whereas CWDRS requires measurements at multiple SDS to have depth resolution [10]. In addition, multiple TRDRS measurements can be used to quickly estimate optical properties without calibration [18, 19]. However, TRDRS systems often require expensive light sources, detectors, and control-electrics as well as careful instrument response calibration [20, 14].

The time response of TRDRS to tissues is an exponential decay in time. The usable signal drops in magnitude by some three decades in less than a nanosecond when measuring the sample. This limits the ability of TRDRS to sense changes at deeper levels in the tissue, because the detectors used have a dynamic range limited to about three decades [21]. The total mean path length of photons, and hence the depth they travel, is proportional to the photon time-of-flight. Thus, if the dynamic range of the detector can be increased, later photons can be resolved that travelled on average deeper in the medium. Recently it has been shown that using time-gated detection in TRDRS can improve the dynamic range of the detector by several orders of magnitude [22, 21, 22]. Further, it was shown that time-gating can increase sensitivity and contrast to absorption changes deep within a scattering medium [23].

A multitude of studies have investigated the estimation of layered media properties from TRDRS or CWDRS measurements [24, 25, 26, 27]. However, none of the studies to our knowledge investigate layered samples using a time-gated detection capable system. In this

2

thesis, it is hypothesized that the increased depth-sensitivity due to time gating will enhance the characterization of properties in the deeper layers of the layered medium. The high-level aim of this research is to use time-gated TRDRS to measure layered samples and to observe if there are any advantages in terms of optical property quantification.

Outline of thesis

The thesis is broken down into four chapters. The first two chapters provide background introduction to the theoretical methods and instrumentation used for DOS with a focus on TRDRS. Chapter 1 provides a theoretical background for the analyses on experiments while Chapter 2 discusses the major building blocks of the TRDRS system used for these experiments. The final two chapters are about the experiments and discussing the meaning of selected data. Chapter 3 is about the materials and methods necessary for setting up TRDRS the experiments that will be discussed. Chapter 4 is a report of the results and interpretation.

Specific objective

Preliminary results have shown that time-gated TRDRS measurements on layered media can match to layered DT for a solid phantom with a single set of optical properties. This result indicates that time-gating definitely has the potential to be used for accurate optical property recovery on larger scale studies with more layered phantoms. The ability to separate the surface layer and the deeper layer optical properties robustly would be very useful for monitoring the concentrations of in vivo chromophores–such as oxygenated or deoxygenated hemoglobin–beneath the skin layer, fat layers or skull layer.

Initially, the aim of this research was to quantify concentrations of chromophores in the deeper layer of a layered medium using time-gated detection and our novel layered DT modeling approach described in briefly in subsection 1.2.4. This would test the ability of the time-gated TRDRS system to quantify changes in concentration of actual in vivo chromophores in deep tissue layers. However, due to technical difficulties that will be discussed in the conclusion, the specific aim of the research became focused on sources of error between the layered DT model and time-gated experimental measurements on layered media.

Specific objective: find the sources of error from time-gated TRDRS measurements on layered media

Two types of layered samples were used for time-gated TRDRS measurements at two SDS and two wavelengths for a total of four measurements for each phantom. The first type of sample tested was a solid in the form of two polymer-based slabs. The DT model predicted the properties of each layer of the solid phantom within a reasonable margin of error.

The second type of phantom tested was in liquid form with the chromophore and scatterer dissolved in aqueous solution and housed in a 3D printed container separating each layer. In the initial test of depth sensitivity range, it was observed that there were significant errors between the layered DT model and the measurements. Additionally, the errors increased as the depth of the top layer of the sample was increased.

Pinpointing the sources of these errors on the liquid layered samples would be critical for determining whether it was the time-gated TRDRS instrument, the DT model or the sample causing the errors. The objective is to test whether these errors could be explained by incorporating an extra thin layer into the DT model. The barrier between the two liquid layers of the sample had a significant thickness of 850 μm and an unknown amount of scattering and absorption. If we show that we can improve the error by simply incorporating another layer into the model, we will know that the DT model can account for thin layers and that the absence of the thin layer in our model caused the error initially. If the DT model incorporating a thin layer does not improve the error, we will have shown that the liquid phantom designed here is not useful for further studies and that such a phantom should be redesigned to fully test the approach of using a layered DT model with time-gated detection.

Chapter 1

Theoretical framework

1.1 Radiative transport equation

The broad theoretical problem in diffuse optics is photon transport through scattering materials. It turns out that the transfer of radiant energy through highly scattering media is best described statistically by an equation called the radiative transfer equation (RTE) [28, 1]. The RTE,

$$\frac{1}{v}\frac{\partial L(\mathbf{r},\hat{\Omega},t)}{\partial t} + \hat{\Omega}\cdot\nabla L(\mathbf{r},\hat{\Omega},t)$$
$$= -\mu_t L(\mathbf{r},\hat{\Omega},t) + Q(\mathbf{r},\hat{\Omega},t) + \mu_s \int_{4\pi} L(\mathbf{r},\hat{\Omega},t)f(\hat{\Omega},\hat{\Omega}')d\hat{\Omega}', \quad (1.1)$$

Table 1.1: The quantities that are used in the radiative transport model with the corresponding symbols and dimensions in SI units.

Symbol	Quantity	Units
$L(\mathbf{r},\hat{\Omega},t)$	radiance	$W\,cm^{-2}sr^{-1}$
$Q(\mathbf{r},\hat{\Omega},t)$	source power/volume	$W\,cm^{-3}sr^{-1}$
$f(\hat{\Omega},\hat{\Omega}')d\hat{\Omega}'$	phase distribution	normalized probability

is centered around the radiance, which is the amount of radiant power per unit solid angle, per projected unit area. The quantities of interest for the RTE are listed in Table 1.1. In Equation 1.1, $\mathbf{r}$ is the position, t is time, v is the speed of light in the medium and $\mu_t = \mu_a + \mu_s$ (the total extinction coefficient) is the loss of radiance due to absorption and scattering *on average* per unit length. The left side of Equation 1.1 represents the change in radiance with time about position, $\mathbf{r}$, propagating in the direction, $\hat{\Omega}$. Due to the conservation of radiant energy, the derivative on the left must be equal to the total gains in radiance minus the total losses in radiance. In the right side of Equation 1.1, the first term covers the loss of

radiance and the next two are the gains from the sources and radiance scattered in direction, $\hat{\Omega}$, respectively.

1.2 Diffusion approximation

There are no closed form analytical solutions to the RTE, but approximate solutions are found by expanding Equation 1.1 to a series of spherical harmonics. This is known as the P_N approximation [2]. Using this approximation is often referred to as diffusion theory (DT). If the radiance is assumed to be isotropic, the series may be truncated at the 2nd term as

$$L(\mathbf{r}, \hat{\Omega}, t) = \frac{1}{4\pi}\Phi(\mathbf{r}, t) + \frac{3}{4\pi}\mathbf{J}(\mathbf{r}, t) \cdot \hat{\Omega}. \tag{1.2}$$

Two new physical quantities are integrated into the two term expansion: the fluence rate, $\Phi(\mathbf{r}, t)$, and the power flux, $\mathbf{J}(\mathbf{r}, t)$. The photon fluence rate is the total power per unit area emitted from an infinitesimal volume at position, $\mathbf{r}$, and time, t. The flux is the vector sum of radiance out of an infinitesimal volume,

$$\mathbf{J}(\mathbf{r}, t) \equiv \int_{4\pi} L(\mathbf{r}, \hat{\Omega}, t)\hat{\Omega} d\Omega. \tag{1.3}$$

For the P_N approximation to hold, we assume that the radiance is nearly isotropic and the distribution of scattering phase only depends on the angle between the incident and scattered light. In other words, $f(\hat{\Omega}, \hat{\Omega}') = f(\hat{\Omega} \cdot \hat{\Omega}')$. Integrating Equation 1.1 over all solid angles results in an equation in terms of the photon fluence rate and the flux,

$$\frac{1}{v}\frac{\partial \Phi(\mathbf{r}, t)}{\partial t} + \nabla \cdot \mathbf{J}(\mathbf{r}, t) + \mu_a \Phi(\mathbf{r}, t) = S(\mathbf{r}, t), \tag{1.4}$$

where $S(\mathbf{r}, t)$ is defined as the total power per unit volume emitted by the source. Equation 1.4 is a continuity equation that simply means that the amount of radiant energy emanating from an infinitesimal volume must equal the amount of light energy that is absorbed or emitted from that volume.

Another relationship between $\Phi(\mathbf{r}, t)$ and $\mathbf{J}(\mathbf{r}, t)$ is obtained when Equation 1.2 is plugged in for $L(\mathbf{r}, \hat{\Omega}, t)$ in the RTE (Equation 1.1). Multiplying everything by $\hat{\Omega}$ and integrating over all solid angles, the RTE in terms of the expansion shown in Equation 1.2 will reduce to

$$\nabla\Phi(\mathbf{r}, t) = -\frac{3}{v}\frac{\partial \mathbf{J}(\mathbf{r}, t)}{\partial t} - 3\mu_t \mathbf{J}(\mathbf{r}, t) + 3\int Q(\mathbf{r}, \hat{\Omega}, t)\hat{\Omega} d\Omega + 3\mu_s g\mathbf{J}(\mathbf{r}, t). \tag{1.5}$$

g is defined as the mean ensemble cosine of scattering angle θ,

$$g \equiv \int_{4\pi} f(\hat{\Omega} \cdot \hat{\Omega}')\hat{\Omega} \cdot \hat{\Omega}' d\hat{\Omega}' = \langle cos\theta \rangle .$$

In other words, g is the probability of scattered light propagating in the forward direction. The typical range of g in soft tissue is from 0.8-0.98 [2].

Assuming the source of radiance is isotropic, the integral of Q in Equation 1.5 is just zero. If it is further assumed that there are slow variations in $\mathbf{J}$ with time, $(1/v)\partial \mathbf{J}/\partial t$ can be neglected compared to $-(\mu_t \mathbf{J}(\mathbf{r}, t) - \mu_s g \mathbf{J}(\mathbf{r}, t))$ in Equation 1.5. The reduced scattering coefficient is defined as the number of random-scattering events per unit length cm^{-1}, $\mu_s' \equiv (1 - g)\mu_s$. Finally, Equation 1.5 simply becomes Fick's law of diffusion,

$$\nabla\Phi(\mathbf{r}, t) = -3(\mu_s' + \mu_a)\mathbf{J}(\mathbf{r}, t). \tag{1.6}$$

The photon diffusion equation is implemented by using Equation 1.6 to rewrite the continuity equation (Equation 1.4) in terms of $\Phi(\mathbf{r}, t)$. We define the diffusion coefficient D as $D(\mathbf{r}) = 1/3(\mu_s'(\mathbf{r}) + \mu_a(\mathbf{r}))$ and let it be the case that the sample is homogeneous, $\mu_s'(\mathbf{r}) = \mu_s'$ and $\mu_a(\mathbf{r}) = \mu_a$. The time-domain diffusion equation becomes

$$\mu_a\Phi(\mathbf{r}, t) + \frac{1}{v}\frac{\partial\Phi(\mathbf{r}, t)}{\partial t} - \nabla \cdot D\nabla\Phi(\mathbf{r}, t) = \delta(\mathbf{r} - \mathbf{r}_s)\delta(t - t_s), \tag{1.7}$$

where the source term is of the form $S(\mathbf{r}, t) = \delta(\mathbf{r} - \mathbf{r}_s)\delta(t - t_s)$ because we assume an isotropic point impulse source (infinitely small in space and time) at point $\mathbf{r}_s$ and time t_s. Equation 1.7, the diffusion equation allows for a quick, approximate model for photon transport in the limit of high scattering ($\mu_s' \gg \mu_a$). As a rule of thumb, it is accepted that the ratio between μ_s' and μ_a should be at least $\mu_s'/\mu_a \geq 10$ [2].

1.2.1 Semi-infinite slab solution

As a simple example of how the DT equation can be solved analytically, the solution for the reflectance–which is the magnitude of the flux at the surface–for a homogeneous, semi-infinite (SI) slab medium [29] is presented below (Equation 1.8, Table 1.2). This particular solution is a classic example that will be used as an illustrative solution case; however, in the research of this thesis we will not use the SI homogeneous medium case.

The diffusion equation is solved for the fluence in this geometry, which can then be used

to find the reflectance as a function of time and radial distance from the source [29]. The reflectance as a function of ρ and t is given by

$$R(\rho, t) = \frac{1}{2}(4\pi Dv)^{-3/2} t^{-5/2} \exp\left(-\mu_a vt\right)$$
$$\times \left[z_0 \exp\left(-\frac{r_1{}^2}{4Dvt}\right) + (z_0 + 2z_b) \times \exp\left(-\frac{r_2{}^2}{4Dvt}\right) \right]. \quad (1.8)$$

Fick's law, Equation 1.6, is used to get the reflectance, $R(\rho, t)$, from the DE fluence [30]. R_{eff} is the fraction of photons that are internally reflected at the boundary and is estimated

Table 1.2: Definitions of the terms introduced to write the closed form solution of the diffusion equation for a semi-infinite slab.

term	definition
ρ	radial distance from source
z_0	$(\mu_a + \mu_s{}')^{-1}$
z_b	$\frac{1+R_{eff}}{1-R_{eff}} 2D$
$r_1{}^2$	$z_0{}^2 + \rho^2$
$r_2{}^2$	$(z_0 + 2z_b)^2 + \rho^2$

to be $R_{eff} = 0.493$ for and medium with an index of refraction of $n = 1.4$ [29].

1.2.2 Green's formula

There is a final step in order to fit the theoretical temporal point spread function (TPSF), generated by theory or simulations, to the measured reflectance–the photon distribution of time-of-flight (DTOF). Since our instruments are not able to measure reflectance relative to a ideal δ function source, the theoretical reflectance must be related to the measured reflectance through a convolution with the instrument temporal response known as the instrument response function (IRF). This is called the convolution theorem that comes from Green's formula,

$$\tilde{R}(t) = \int s(t')R(t - t')dt'. \quad (1.9)$$

With Equation 1.8 and 1.9 in hand, the DT reflectance can be computed for any input optical properties. With a measured IRF, the convolved theoretical reflectance may be iteratively fit to the measured reflectance of diffusive tissue mimicking sample. The particular DT equation solutions that will be used in this thesis are the finite slab solution (subsection 1.2.3)

for estimation μ_a and $\mu_s{}'$ for single solid slab samples and the N-layer cylinder solution (subsection 1.2.4), which was the basis for our layered diffusion-based model studies.

1.2.3 Finite slab solution

A previously described [31] DT solution for a slab geometry of finite thickness was used in this study to characterize the top layer of a solid-state polymer slab sample. The time-resolved transmittance measurements were fitted using the time-dependent diffusion equation for thin slab [31] and numerical convolutions with the respective IRF for each wavelength. In the inverse-fitting, a time-shift parameter was included to fit alongside μ_a and μ_s' to account for time delays from the IRF measurements.

1.2.4 N-layered cyclinder solution

For the layered samples, solutions to the diffusion equation for an N-layered finite cylinder was used (with N=2) to calculate the reflected photon fluence on the top boundary ($z = 0$) [32]. The time-dependent fluence rate was calculated by numerically inverting the Laplace transform of the steady-state layered diffusion equation [33, 34]. The reflectance was calculated as a function of SDS using Fick's law [31]. A cylinder radius of 10 cm was used to approximate laterally infinite boundaries.

1.3 Time-of-flight moments

A quick way to characterize tissue mimicking samples without fitting to TPSF convolutions is to calculate the time-of-flight moments of the measured DTOF [35]. This technique will be used towards the end of the analysis chapter in section 4.3 to investigate methods for avoiding diffusion model error. For simple geometries–the infinite medium (IM) or SI medium–the measured moments themselves can accurately and efficiently estimate optical properties directly, given a sufficient SDS and assumed homogeneity of the sample.

In this study we will rely on the a so-called "subtraction" method of moments [19], that has the advantage of effectively eliminating the impact of the IRF and associated TPSF convolution to DTOF time delay [35]. the standard formula for the normalized moment of order k for the distribution $g(t)$ is as follows

$$m_k = \langle t^k \rangle = \frac{\int_\infty^\infty t^k g(t) dt}{\int_\infty^\infty g(t) dt}. \tag{1.10}$$

The moments defined by Equation 1.10 are centered about the origin, which is set by either the mean or the peak of the IRF of the system [35]. μ_s' and μ_a are calculated directly from DT using the 1st and 2nd *centralized moments*. The first centralized moment, $k = 1$, is simply the mean time of flight. The second centralized moment, often called the "variance", is a measure of the spread of the distribution *about the mean*. The variance can computed directly from the 1st and 2nd moments as $V = \langle (t - \langle t \rangle)^2 \rangle = m_2 - m_1^2$.

Using the subtraction approach, the difference of the 1st and 2nd centralized moments are taken at two separate SDS. This subtraction should wash away the IRF shape and also put the moments in terms of a relative time. We used the differences of the 1st and 2nd central moments to estimate the reduced scattering coefficient in our study, so that it can either be used as a parameter for fitting or a test of our sample calibration principles. μ_s' can be defined in terms of the changes in moments as

$$\mu_s' = \frac{2v\partial m_1^3}{3\partial V \partial r_{SDS}^2}. \tag{1.11}$$

Equation 1.11 directly estimated μ_s' from changes in moments with SDS using IM Diffusion Theory [19]. v is the speed of light in the medium, ∂m_1 is the change in mean time of flight, ∂V the change in variance and ∂r_{SDS} the change in SDS.

Chapter 2

Instrumentation

At a high-level, a TRDRS system is made up of a light source, a sample and a detector. The light source is coupled to the sample while the detector is set up to detect diffusely back-scattered light (reflectance). This chapter will be about the details that distinguish our TRDRS system from the more familiar spectroscopy setups.

Figure 2.1 illustrates the components necessary to build the specific TRDRS system we have with detector time-gating capabilities. A pulsed laser, with a less than 100 picosecond pulse width, is used for the light source. The broadband pulsed laser central wavelength and bandwidth are tunable using a directly coupled acousto-optic tunable bandpass filter (AOTF). The source optical power is selectively attenuated using a variable optical attenuator made out of reflective neutral density filters (Newport Corp., Irvine, CA, USA). Light is coupled to and from the sample using multimode optical fibers in direct contact with the sample.

Most state of the art instruments use single-photon counting detectors, which could be either single-photon avalanche photodiodes (SPAD)s or photomultiplier tubes (PMT)s. In this research, a SPAD detector is used. One of the fibers in contact with the sample is coupled directly to the SPAD's 50 μm diameter active area. For time-gated TRDRS, the detector must be electronically coupled in series with a picosecond delayer and a control unit, *CU*, for moving and applying the gate voltage respectively. The laser pulse trigger output is in connection with the time-correlated single photon counting, *TCSPC*, module and also the delayer and CU if gating is necessary [36]. If gating is not needed, the TRDRS system setup will be the same as in Figure 2.1, but without delay and CU connected in series with the SPAD. The following sections will go into more detail on the main components of the TRDRS system; namely, the laser, the detector plus gated control electronics, and the TCSPC module.
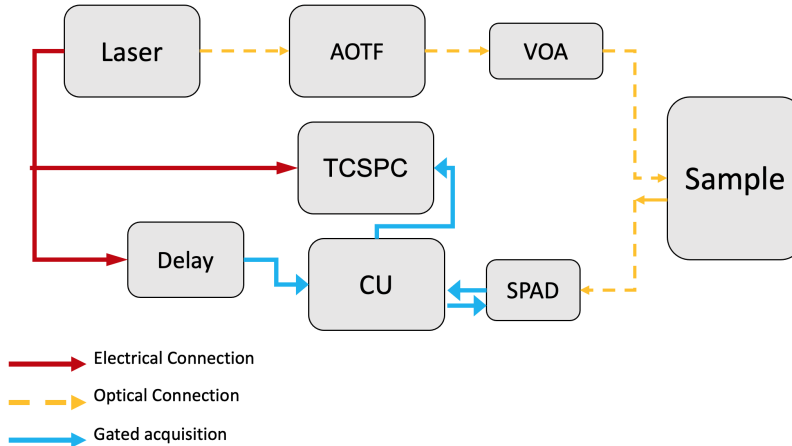
Figure 2.1: The TRDRS experimental system built around a unique supercontinuum fiber laser, *SPAD* single photon-avalanche photodiode; *AOTF*, acousto-optic tunable bandpass filter; *VOA*, variable optical attenuator; *TCSPC*, time-correlated single photon counting module; and, *CU*, control unit for the SPAD bias voltage. The system illustrated by this schematic was designed and made in our lab.

2.1   Supercontinuum fiber laser

In order to do TRDRS as opposed to CWDRS, the light source must be pulsed with a pulse width at or below about 200 picoseconds [20]. TRDRS measurements are on the 0.1-10 nanoseconds timescale [37]. Picosecond pulse-widths are close enough to delta impulse functions on this timescale to resolve the pulse-broadening due to the scattering and the absorption properties of tissues.

The three main types of ultrafast lasers used for TRDRS in the laboratory are Ti:Sapphire solid-state lasers, pulsed diode lasers and photonic crystal fiber lasers. TRDRS experiments using ultrafast dye lasers have also been reported [14]. Noticeably, each type of laser mentioned is bulkier, more expensive and more cumbersome (long warm-up times/less power stability) compared to available sources for CWDRS systems, which are usually broadband halogen lamps or wideband LEDs [20, 3]. Due to these drawbacks of TRDRS light sources, there are far less commercial TRDRS systems available [14]. Technological advances in TRDRS light sources in particular may serve to make systems more compact, portable and inexpensive, leading to wider use of the technique in clinical research settings, with more commercial systems available on the market.

Among these pulsed lasers, supercontinuum (SC) fiber lasers have become a popular choice due the modernization of supercontinuum generation [38]. Our system specifically uses a SC fiber laser (Fianium SC400-4, NKT Photonics, Denmark). In this section we will briefly discuss how these light sources operate and why they are useful for clinical and translational research applications.

2.1.1 Supercontinuum generation

The contents of the section are mainly a review of a web page article found on rp-photonics [39] and a review of the use of supercontinuum (SC) in diffuse optical spectroscopy [38]. Supercontinuum (SC) generation is a nonlinear optical process in which narrowband laser light is spread out into a continuous and wide optical spectrum. In theory, the high spatial coherence of a laser can be used to our advantage while now having a continuous and broad spectrum.

SC generation can be achieved with light propagating through any nonlinear medium. Even water can be used for SC generation, which was demonstrated in early hyperspectral TRDRS research [13]. However, the efficiency of the input light pulse power versus output power is very low for most generic materials. In addition, the pulse power is spread out over the entire spectrum, making the pulse at a particular wavelength too low in energy to be useful.

Photonic crystal fibers are a special type of fiber, usually made from fused silica, that guides light solely base on the effective refractive index due to a unique microstructure. Figure 2.2 shows the structure of photonic crystal fiber with a hexagonal pattern of air holes used for the nonlinear medium. The characteristic chromatic dispersion of these fibers over a long enough length will lead to SC generation at a much lower power than for less exotic media such as water. hence most SC generation is now commonly accomplished using specially designed photonic crystal fibers.
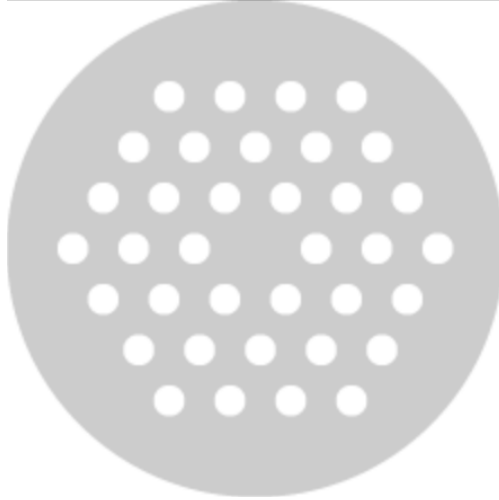
Figure 2.2: A cross section of typical glass photonic crystal fiber with hexagonal pattern of air holes. Air hole diameter is on the scale of a few micrometers. Image courtesy of rp-photonics [39].

The mechanism for picosecond pulse SC generation is dependent on the chromatic dispersion of the medium, length of fiber, pulse duration and peak power of the pump laser. Raman scattering and four-wave mixing, are the key nonlinear optical effects behind the process.

SC fiber lasers are useful in TRDRS clinical research because they have a wide, high power density spectrum in the visible to NIR range. In addition, they are more robust and more compact as compared to the earlier Ti:Sapphire lasers and pulsed dye lasers. This allows for portable systems that can be carried in carts, with no limitations on wavelength choice, instead of setups on a heavy table top that either have limited and slow wavelength tuning or a completely fixed wavelength [14, 20]. The broad spectrum of SC fiber lasers can be enjoyed for quick switching of discrete wavelengths using tunable bandpass filters or prisms. In addition, the entire fiber laser spectrum can be harnessed all at once for hyperspectral TRDRS [13].

2.2 Single photon avalanche photodiode detectors

A SPAD is basically an avalanche photodiode (APD) with a special quenching circuit to reset the APD bias conditions after an avalanche is triggered. An APD is a photodiode operated in "Geiger" mode, with the reverse bias voltage greater than the breakdown voltage. A basic circuit diagram of a SPAD that does not go into the details of quenching circuit is shown in Figure 2.3. The next section will delve into more details about requirements for SPAD design. This section provides a review of several key references detailing SPAD operation
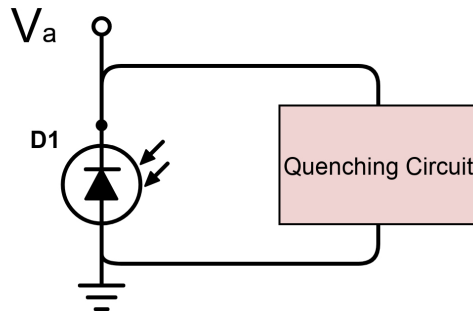
[40, 22, 21].

Figure 2.3: A SPAD schematic at the most basic level. V_a is the bias supply voltage, D1 is the photodiode. This is a diagram illustrating SPAD principles of operation is not illustrating a circuit that needed to be built in the lab.

2.2.1 Operating conditions for SPADs

The two main conditions affecting SPAD behavior that can be controlled are the temperature and the bias voltage. SPADs are also affected differently by the conditions if they are fabricated differently. For this section, the details of SPAD fabrication will be avoided as the SPAD type can be broadly grouped into either a thin junction SPAD or thick junction SPAD for simplicity. The affects of SPAD temperature and bias voltage on SPAD performance will also be discussed.

The thickness of the insulating SPAD junction depletion layer is typically from 20-150 μm for thick junction SPADs and about 1 μm for thin junction SPADs. The thickness of the depletion layer dramatically affects the properties of the breakdown voltage, active area, detection efficiency and photon timing resolution [40]. Table Table 2.1 summarizes the common properties of each type of SPAD.

Table 2.1: The features of thick junction and thin junction SPADs in general. These parameters were summarized from Cova et al. [40].

	Thin junction	Thick junction
Breakdown voltage	10-50 V	200-500 V
Active area diameter	5-150 μm	100-500 μm
Detection efficiency	45% at 500 nm; 10% at 830 nm	50% over 540-850 nm
Timing resolution	<100 ps FWHM	<350 ps FWHM

We define the excess bias voltage, V_E, of the SPAD as $V_E = (V_A - V_B)$, which depends on the diode breakdown voltage, V_B, and the bias voltage, V_A. Changing the amount of excess bias voltage dramatically affects the performance of the SPAD in terms of detection efficiency, timing resolution, dark-count rate and heat dissipation. As expected, the detection efficiency of the SPAD increases with increasing V_E because the avalanche triggering probability is greater at higher V_E. Likewise, the timing resolution improves with increasing excess bias, because of the stronger electric field induced, which accelerates charge carriers across the SPAD junction more quickly.

Like PMT detectors, SPADs can trigger current pulses even in complete darkness due to thermal effects. This thermally generated noise is known as the dark count rate (DCR). Unfortunately, DCR increases exponentially with increasing V_E. This is due to the field-assisted carrier emission from the generation sites in the SPAD junction, which again increases the triggering probability.

A secondary form of DCR noise occurs when carriers get trapped in the SPAD junction depletion layer during avalanche. At a randomly varying time delay, the trapped carriers are released and trigger more dark avalanches, which significantly increase the DCR nanoseconds after the actual light pulse was detected. Afterpulsing also increases with V_E because the number of trapped carriers increases with increasing avalanche current, which is proportional to V_E.

As the working temperature of the SPAD junction increases, the breakdown voltage V_B, increases. This means that the V_E and, as a result, the detection efficiency fluctuates with temperature. Each time an avalanche is triggered, there is a significant amount of heat dissipation, so there is a tendency for the SPAD to increase temperature that is proportional to the mean counting rate. For this reason it is necessary to keep the junction at a steady working temperature using an accurate thermoelectric cooler.

2.2.2 Quenching circuits

One way to quench the breakdown avalanche is to use what is called a passive quenching circuit (PQC). The name of this quenching technique comes from the way the circuit uses the avalanche to quench itself over time. The basic design of a PQC is shown in Figure 2.4.

When the avalanche is triggered, the voltage signal is sensed by a fast comparator, which produces an output pulse "click" for counting. The SPAD avalanche can be illustrated using a simple equivalent circuit with a diode capicitance C_d, and diode resistance, R_d, shown in Figure 2.4a. The diode in the quiescent state is like an open switch, with the anode being

at low voltage. When there is an avalanche, the switch is closed and the anode comes into connection with the bias voltage, producing a quick transient voltage spike. Because of the large ballast resistor, R_B, the PQC makes the voltage on the cathode decay back to the quiescent level, as C_d discharges, and the SPAD is then reset over time. A circuit diagram showing the basic principle of PQCs with a ballast resistor is shown in Figure 2.4.
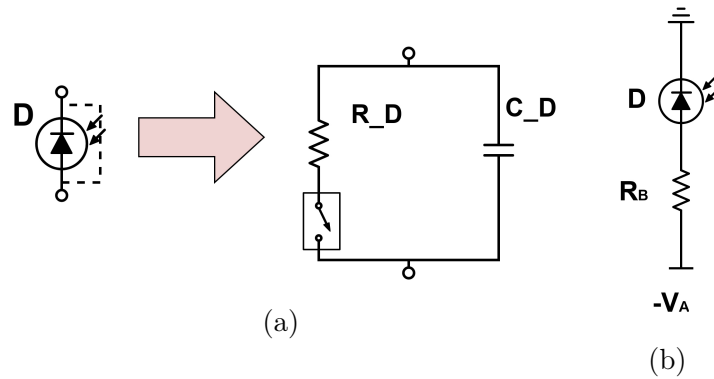

(a)

(b)

Figure 2.4: Figure 2.4b is the general PQC with a high impedance balance resistor R_B that drops the voltage across the junction back to near the breakdown to quench. Figure 2.4a is a simple equivalent diagram illustrating the diode in the dormant and avalanche state using a switch, diode capacitance C_D and resistance R_D. This diagram was made using open-source circuit diagram software (digikey.com). The actual circuit was not itself built in the lab; adapted from Cova et al., © 1996 Optica Publishing Group, DOI: AO.35.001956 [40].

PQCs were used in the earliest studies of photodiode avalanche phenomena and are still in use, however they cannot be used in high count rate applications because of the quenching time constant is on the order of microseconds. In fact, the photon counting and timing performance of PQCs is not high enough for photon counting/timing applications when the count rate goes beyond a few hundred kilocounts per second [40].

Active quenching

To overcome the limitations of PQCs and exploit the benefits of SPADs, the active quenching circuit (AQC) was developed. Figure 2.5 below is a circuit diagram, adapted from Cova et al. [40], that illustrates the main principle of AQCs.
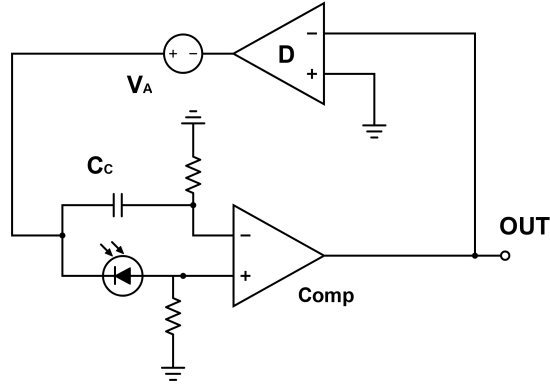
Figure 2.5: Principle mechanism of an active quenching reset circuit. When the SPAD is triggered, The differential input of the comparator triggers an output that can be used for counting and also is used by a reset driver to quench the SPAD. Adapted from Cova et al., © 1996 Optica Publishing Group, DOI: AO.35.001956 [40].

The avalanche signal is picked up by a coupling capacitor, C_c, and sensed by the input of a fast comparator. The ouput of the comparator goes to a reset driver, D, that changes the reverse bias voltage back to breakdown voltage, (V_B), or below. The reset driver keeps the bias voltage around V_B for an accurately controlled hold off time. SPADs with AQC front end can reach count rates in the millions of photons per second, limited mainly by the hold off time.

2.2.3   SPAD gating circuit

Although the AQC is used almost exclusively in modern SPADs, the AQC is not appropriate for fast gating of a SPAD. This is because of the stray capacitance and the limited drive current of the integrated circuitry of typical AQC approaches, which limit the gate transitions to a few nanoseconds (too slow for timing resolution required for TRDRS). Instead, a modified version of the PQC is used in which the ballast resistor is replaced by a wide-band bipolar transistor capable of fast quenching the SPAD when the transistor is forward biased. Thus the quenching circuit for gated applications is "passive", but it is capable of sustaining high count rates due to the high speed of the reset transistors.

Coupling capacitors are used at the avalanche voltage comparator input, in order to block the voltage of the gate from getting passed to the comparator. However this coupling cannot remove spurious voltage spikes from the gate voltage ringing. These spurious voltage spikes are three times the size of the actually avalanche voltage, so photons will go undetected in this gating arrangement. Additionally, fast pulse generators used for applying the gate

18

usually have small overshoots and oscillations around the gate voltage. These oscillations will get amplified by the exponential relation between V_E and SPAD efficiency. In order to overcome these drawbacks, a new gating circuit was developed with a very stable applied voltage gate and a "dummy" capacitor channel that mimics the SPAD capacitance. The dummy capacitor mimics the spurious voltage peaks, which are then superimposed on the actual spurious voltage peaks at the comparator differential input [22]. Figure 2.6 is a schematic that illustrates the recently proposed fast gating and quenching circuit.
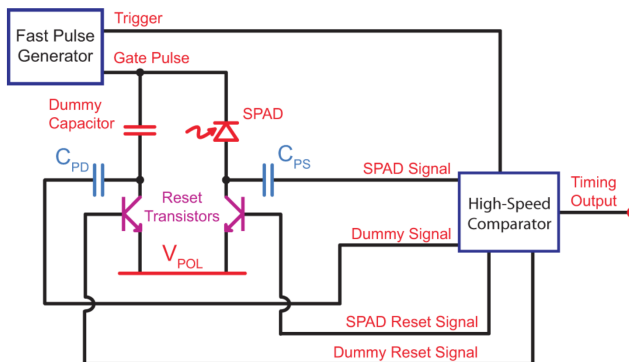
Figure 2.6: The principle mechanism of SPAD fast gating. A passive quenching circuit with the ballast resistor replaced by a wide-band bipolar junction transistor. An extra channel with a "dummy" capacitor and coupling capacitor is needed to detect photons when the gate is on, after the dummy capacitor voltage spikes are superimposed on the spurious gate voltage spike [22]. © 2011 IEEE. Reprinted with permission.

2.3   Time-correlated single photon counting module

Most of the time in TRDRS, SPAD or PMT detectors are used due to being more compact, less expensive and less susceptible to damage from overexposure or gating, as opposed to streak cameras or charge coupled device (CCD) cameras with an intensifier [20, 36, 22]. PMTs and SPADs are photon counting detectors and thus require the use of TCSPC to quickly record the frequency of each photon arrival time, for use in TRDRS systems. In this section, the general principles, structure and optimization of TCSPC systems will be discussed. The contents of this section are largely a review of important TCSPC references [41, 42, 43].

2.3.1 General TCSPC principles

The result of TCSPC is a histogram of photon arrival time frequency. Figure 2.7 shows a schematic of the photon arrival time frequency distribution that is a result of counting a random sample of photon arrival times. Unlike gated photon counting methods where a narrow gate is shifted and the measured time-window is shifted over the region of interest, TCSPC acquires the entire arrival time distribution over the whole pulse period of the laser source [41]. TCSPC builds this distribution by communicating with a single photon detector, making sure the photon count rate of the detector is less than 10% of the laser repetition rate. So long as the count rate is low enough, the probability of detecting more than one photon each pulse period is negligible.

After a single photon is detected, the time of the detected photon is measured by the timing circuit. Each arrival time event is recorded in the memory by adding an event to the memory address location that is proportional to the arrival time (Figure 2.8). With a high repetition rate laser, state of the art TCSPC systems can count photons accurately at 1 or more million photons per second, allowing a useful signal to build up in the memory in seconds or less.
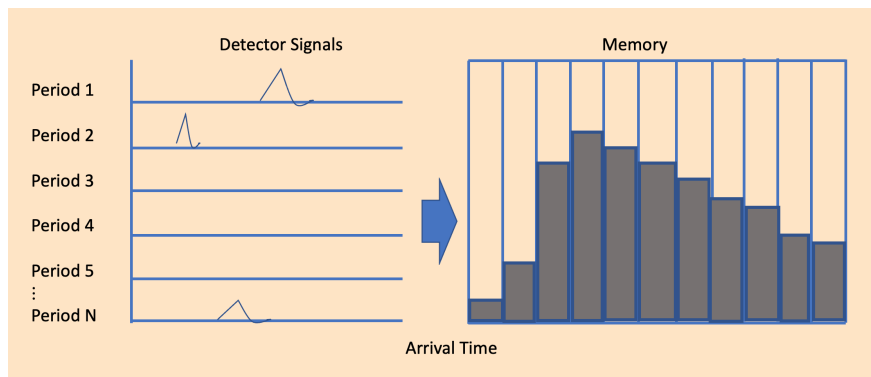
Figure 2.7: Photons are counted at a rate of < 0.1 photons per period (not accurately shown here for illustrative purposes). Arrival times for each photon are measured and located according to arrival time in the memory. This schematic was adapted with permission from W. Becker, © 2005 Springer [44].

2.3.2 Components of advanced TCSPC systems

The basic flow of a TCSPC system starts with the detector sending pulses to an input discriminator. The discriminator is effectively a comparator that counts pulses with an amplitude above a programmable cutoff level. The particular discriminator used for TCSPC

is called the constant fraction discriminator (CFD), which is crucial for preventing timing jitter as will be discussed in subsection 2.3.2.

The reference pulses from the source, known as the "synchronization" output or "trigger out", are also connected to another CFD. Together, the reference CFD output and detector CFD output are used as the start and the stop signals for the time-to-analog converter (TAC). The TAC puts out an analog signal with a final voltage proportional to the amount of time between the start and the stop signals. The basic TAC circuit works like a switched current that charges a capacitor–while keeping the current constant–when switched on.

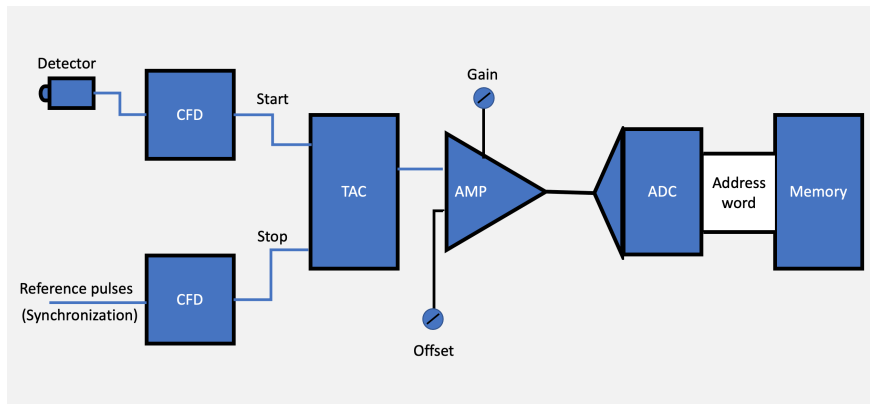Figure 2.8: A general TCSPC schematic with two constant fraction discriminators, *CFD*s, connected to the detector and the reference trigger outputs. The CFD outputs go to the time-to-amplitude converter, *TAC*, and an amplifier, with a gain and an offset input setting, which amplifies the TAC output. The analog-to-digital converter, *ADC*, reads the TAC output and correlates the output voltage with the arrival time, transmitting a digital word whose address is a location in the memory that correlates to the photon's measured arrival time. This schematic was adapted with permission from W. Becker, © 2005 Springer [44].

After the TAC output comes a biased amplifier (AMP) that allows a smaller time window to be selected, without increasing resolution, by increasing the AMP gain. The AMP also has an *offset* setting that results in shifting the delay of the measured arrival times with respect to TAC time-zero reference point.

The amplified TAC output is connected to the analog-to-digital converter (ADC), which encodes the TAC output signal into a digital equivalent. It is especially important that the ADC be very precise to parse the TAC output into several thousands of time-bins of uniform bin width. If there is any non-uniformity in binning, the arrival time distribution will get systematically distorted.

The output of the ADC is an address word that is addressed to a specific time bin location in the memory. An adder adds each output word one by one to the appropriate

memory location. Over time, the total time-of-flight histogram is built up cumulatively in the memory. The entire process of TCSPC in general is summarized by Figure 2.8.

Reversed start-stop

For high-repetition rate sources, from 50 MHz–100 MHz, it is necessary for the system in Figure 2.8 be in the "reversed start-stop" configuration. This is why the start signal comes from the detector CFD output pulse and the stop signal comes from the reference (sync) CFD output pulses. If the configuration is such that the synchronization pulses are the start signal and detector signals the stop, there would be many pulse periods when the TAC would be started but not stopped. For low-repetition rates, it is feasible to include a reset circuit that resets the TAC if no photon is counted in the range of the pulse period; however, making the detector CFD output the start signal guarantees that the TAC gets started only if a photon arrival event is detected. The time will be measured from the photon arrival signal until the next sync output pulse signal is sensed by the reference CFD to stop the TAC [41].

Constant-fraction discriminators

Simple leading-edge discriminators are not optimal for TCSPC because they introduce significant time jitter. The time jitter actually arises from an amplitude jitter associated with SPADs and PMTs due to their random amplification methods. CFDs trigger at a constant fraction of the detector pulse amplitude, avoiding the amplitude jitter and thus time jitter.

New CFDs have a rather simple design thanks to the availability of fast comparator chips based on emitter-coupled logic (ECL). The differential inputs of the comparator are used to trigger the CFD at the baseline transition of superposition of an input pulse and the delay of that input pulse. The differential input subtracts the delayed pulse from the original pulse while the trigger level is set close to zero as shown in Figure 2.9.
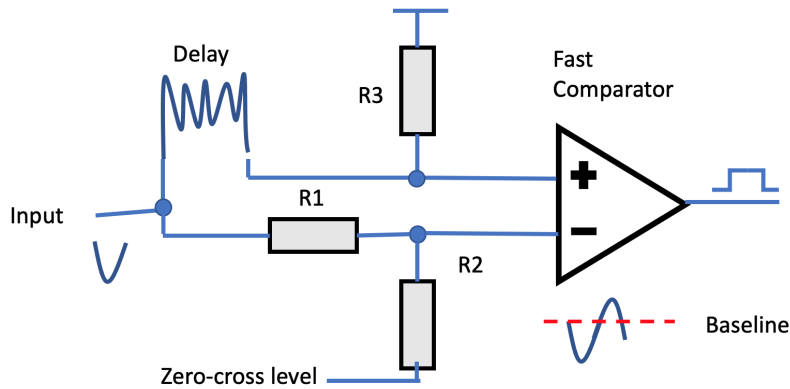
22

Figure 2.9: The CFD comparator triggers when the differential input crosses the zero baseline which can be adjusted by the zero-cross voltage and load resistors R1 and R2. This schematic was adapted with permission from W. Becker, © 2005 Springer [44].

The shape of the pulse and the delayed pulse superposition can be adjusted using different load resistors and by changing the "zero-cross voltage" (Figure 2.9). The output pulse of the fast comparator is ideally independent of amplitude; but, in reality there are additional circuits to prevent spurious triggers due to the differential input trigger oscillating around zero [44].

Time-to-amplitude converter mechanism

The general setup of advanced TAC systems used for TCSPC includes two fast flip flops, $FF1$ and $FF2$, connected to two separate switches, $S1$ and $S2$, that lead to a charging capacitor, C (see Figure 2.10). When there is no start or stop signal, the switches are held in the "off" state by the flip flops and the current I_s flows through $S1$ and $S2$ directly to ground. When the start pulse from the detector CFD output comes to the $FF1$ input, $S1$ is kept in the "on" state and steady current I_s charges timing capacitor C, linearly increasing the voltage.

The stop signal comes from the next sync CFD output and it sets FF2, turning S2 to the "on" state. Now current I_s is discharged directly to ground while the voltage of capacitor C remains constant. Finally, after the final voltage left on capacitor C is sampled by the ADC, the circuit resets both flip flops and capacitor C gets discharged.
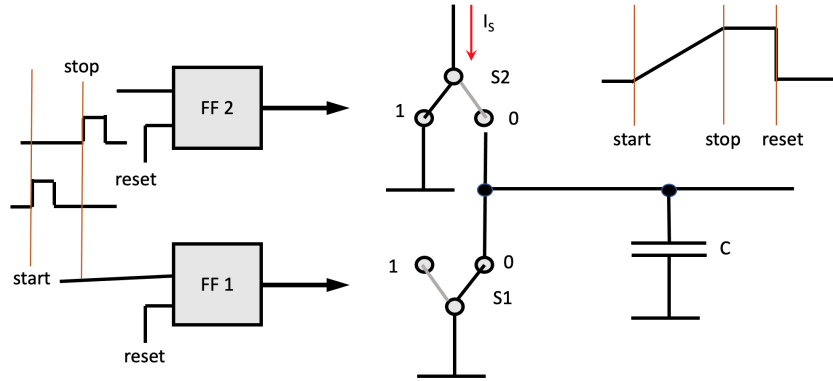
Figure 2.10: General TAC system: the leading edge of the start CFD output, coming from the detector, sets the first flip flop, $FF1$. $FF1$ turns switch 1 ($S1$) on and starts the steady charging of timing capacitor, C. The leading edge of the stop CFD output, coming from the synchronization, sets flip flop 2 ($FF2$), which flips the state of switch 2, $S2$, sending constant current I_s to ground. After the ADC reads the voltage at C, there is a reset circuit that resets each flip flop which sends I_s and C to ground. This schematic was adapted with permission from W. Becker, © 2005 Springer [44].

Building a TAC realistically requires several electronic components. First, the switches are made from transistor pairs to limit oscillations. In addition, the flip flops must be fast ECL delay flip flops. Next, additional circuits keep the voltage across the current source steady. Finally, circuits to reset the flip flops, holding the reset state until the capacitor fully discharges are required [42].

Analog-to-digital converter

In the past, the ADC has been the major bottleneck because of the inherent speed-accuracy trade-off. Current TCSPC systems operate with 12-bit ADCs, using a fast error correction method that was modified from a process call "dithering". Fast 12-bit ADC circuits can be used with modified dithering because the small inaccuracies in address word location become random and can be averaged out. To do this type of dithering, a binary counter is connected to the photon counting detector CFD output to control the DAC. The DAC produces a sawtooth signal as the counts increase and then the count is reset. This analog voltage signal, called the "dither voltage" (V_{dith}), is added to the TAC output voltage that is converted to an address word by the ADC. The memory is also connected to the binary count in parallel to the DAC, so that the binary word for the V_{dith} can be subtracted from the ADC output address word.

An important feature of the ADC circuit is that the number of time channels can be changed, altering the resolution of the waveform. If less resolution is required, the ADC can be set to have less time-channels so that multiple ADC channels can be assigned to a single time channel. This builds up a higher signal in less time, at the expense of time resolution. There is also the "ADC Zoom" feature that allows all of the ADC channels to have their own separate time channels within a specified time range. Decreasing the time range via the ADC Zoom increases the time-resolution.

2.3.3   TCSPC settings in practice

There are two important settings for optimizing the detector CFD in real systems, the CFD threshold and zero-cross level.

The CFD threshold sets the minimum voltage of the input signal that will be sufficient to trigger the CFD. If the threshold is too low, noise from the detector will broaden the IRF and if it is too high the CFD input will get killed before even getting to the fast differential comparator (see Figure 2.9). It is best to strike a balance between the broadening of the IRF and the decrease in count rate. This can be achieved by choosing a detector CFD threshold level where there is a plateau in the count rate versus threshold distribution [43]. In other words the threshold setting is high enough to kill the rush of detector pulses from noise (which have lower amplitudes), but wiggling the threshold up and down does not alter the detector CFD count rate significantly.

The zero-cross level is the offset voltage setting that controls when the CFD is triggered from the crossing level of the pulse and delayed pulse signal difference (see Figure 2.9). The intrinsic delay of the CFD input in practice has an amplitude-dependent time-jitter, which leads to a further time-jitter from the triggering of the fast comparator [43]. Setting the zero-cross level slightly above or below the baseline will minimize this time-jitter because the comparator will be triggered by the steep-slope portion of the input/difference signal. Issues can happen when the ZC-level is too close to the baseline level, which can cause the discriminator to trigger spuriously at the synchronization channel [43]. Additionally if the ZC-level is too high, along with a low CFD threshold setting, the threshold discriminator may trigger while the zero cross discriminator does not, so the CFD pulses get killed even if the threshold discriminator indicates a count rate.

The transit time of the input pulses of the detector and the reference channels needs to be properly adjusted so that the phase of the signal is in the TAC range. The way to increase or decrease the transit time of either channel is to add or remove cable 1 meter at

a time, which corresponds to a delay of close to $\pm$ 5 nanoseconds. For lasers with constant repetition rates and low pulse-to-pulse jitter, it should not matter if the stop pulse is from a different pulse than the one that excited the detection pulse. However, it is necessary that the reference pulse must be delayed so that it arrives after the photon detection pulse from the same period. The right delay of the reference channel would be the detector channel transit time, plus the width of the recorded time interval, plus a few nanoseconds for the TAC start delay.

Below the table shows a summary of TCSPC settings that have been found to work in our research.

Table 2.2: System parameters for using the fast-gated detector and TCSPC module.

TCSPC Setting	Effect	Typical Ranges
CFD limit low	detector discriminator threshold	-50.98 mV
CFD ZC level	zero cross level detector CFD	9.83 mV
ADC Resolution	number of time bins	4096
Dither range	amplitude of dithering	1/32 (of ADC input amplitude)
TAC range	length of TAC timing range	5E-08 s
TAC Gain	Zoom	1
TAC Offset	Fine tune signal alignment	5.10 %
TAC limit low	lower limit of TAC voltage	3.92 %
TAC limit high	upper limit of TAC voltage	94.90 %
Sync ZC level	zero cross level sync input CFD	-9.83 mV
Sync Freq Divider	divides sync output pulse frequency	1
Sync threshold	threshold of sync input CFD	-50.98 mV

2.4   Gated TRDRS

With the current TRDRS system (Figure 2.1), we were already in possession of a laser source, AOTF, and a free-running, actively-quenched thin-junction SPAD with TCSPC for detection. Now, it would seem that all we need is a fast pulse or "gate" generator with a programmable delayer. However, it was found that without the proper SPAD analog front-end electronics, the time-of-flight signal will have too many oscillations and ringing due to the sub-optimal bias voltage during the gate-on, gate-off transitions (subsection 2.2.3) [36, 22]. As such, a commercially available SPAD [45] with a control unit (CU) were ordered for coupling to the programmable delayer and TRDRS system. Figure 2.11 shows an image

of the FastGatedSPAD (FGSPAD) and control unit (Micro Photonic Devices [MPD], Italy).

(a)   (b)

Figure 2.11: Figure 2.11a shows an image of the programmable delayer used in our system. Figure 2.11b shows the control unit coupled to the SPAD detection head with a wide-bandwith cable

2.4.1 SPAD control unit and delayer settings

The delayer, CU and SPAD must be connected as shown in Figure 2.1 (blue arrows) in order to have a time-gated TRDRS system. There are also important required settings to make sure these instruments communicate properly. This section will go into more detail on these settings, similar to subsection 2.3.3 for TCSPC. All of the information on the proper settings was obtained from meeting with a technical specialist from MPD who was a developer of the FGSPAD system.

For time-gated TRDRS, the laser pulse synchronization (sync) output not only goes to the TCSPC sync input CFD, but also it has to be split by an impedance-matched splitter and sent to the programmable delayer. The delayer, like the TCSPC module, has an input discriminator that needs a threshold setting. Additionally, the delayer has settings for the output pulsewidth and whether the discriminator is triggered by the rising or falling edge of the input trigger. The delayer threshold setting should in theory be the same as the TCSPC reference CFD threshold; however, it was found from trial and error that the delayer trigger input can only "see" the synchronization pulses when it is set to 30 mV. This is because the splitter significantly degraded the dynamic range of the sync pulses from ~120 mV to ~40 mV.

The pulsewidth setting of the delayer does not actually matter as long as it is below 25 nanoseconds, which is the pulse period of the 40 MHz laser. Whether the delayer discriminator gets triggered by the rising or falling edge of the sync pulse does not matter either.

All that will change is that there will be a finite time shift that can be programmed away by the delayer unit. Table 2.3 is a summary of the gating settings.

The output of the delayer is used as a trigger for the CU to apply the gate voltage. The delayer output is triggered by the laser sync output pulse and also now has a programmable delay. The trigger threshold of the CU should be set to -300 mV because the delayer output has a dynamic range from roughly -600 mV. The CU also controls the working temperature of the SPAD junction, the hold-off period of the quenching circuit, the SPAD excess voltage V_E, the avalanche threshold and the diode current.

The FGSPAD is a thin junction SPAD with a 50 μmactive area diameter. As such the settings given in Table 2.3 are necessary. The CU is connected to the SPAD, along with the front end quenching, gating and cooling circuitry by a large bandwidth cable that sends data to and from the SPAD and CU. The avalanche triggers an output pulse that is sensed through the control unit. The output of the CU is then sent to the detector channel CFD input of the TCSPC module. The CFD threshold of the detector CFD input is optimized as in Table 2.2 using the TCSPC system parameters settings.

Table 2.3: The necessary settings for the FGSPAD and control unit recorded from meeting with the technical specialist and troubleshooting in the lab during the setup process.

Gate setting	Effect	Reference Ranges
delayer threshold	delayer trigger out	30 mV
delayer pulse width	output pulse duration	8 ns
CU threshold	CU trigger out	-300 mV
avalanche threshold	jitter	16 mV
photocurrent	transition speed	80 mA
V_E	sensitivity	5V
temp	background noise	25 °C
hold Off	afterpulsing	150 ns
gate width	duration of gate	>5 ns
gate delay	gate alignment	steps of 10 ps

The avalanche threshold is the voltage needed to create breakdown in the reversely biased photodiode. Increasing it will make the photon time-of-flight distribution have a more precise form. there will be less oscillations; however, there will be more jitter, or deviations from the ideal periodicity of the signal. The photocurrent will make the signal response faster and increase resolution, but will also decrease the precision of the signal form (increasing oscillations).

The temperature parameter is of essence for keeping the detector at reasonable work-

ing temperatures, because the thermal effects can make the DCR, V_E and thus detection efficiency fluctuate. Temperature is controlled by a compact Peltier cooler.

It is necessary to keep the hold off time around 150 ns so that the SPAD can be quenched and again reverse biased, while also minimizing afterpulsing [40].

The most programmable parameters of the gated detector are the gate width and delay. The gate width can range from 2.0-8.0 nanoseconds. Decreasing the width decreases the count rate of detector dramatically, as the detector operates for a smaller portion of the pulse period. This may be useful in measuring the arrival times of the early arriving photons. For the later arriving photons, a larger gate width is ideal to increase counts and decrease collection time. The gate voltage can be delayed with a step size down to 10 picoseconds precision using the programmable delayer.

2.4.2   Reconstruction code

Gated TRDRS measurements start with the rising edge of the optical gate coming before the peak of the pulse. The gate is then delayed such that the rising edge cuts into the pulse peak by ∼50-100 picoseconds, using the picosecond delayer. Often a large set of delays are taken [22]; we usually go in steps of 250 picoseconds to ensure that the transient broadening of the optical gate and detector response, which is time-variant [46], can be discarded using a reconstruction code.

Figure 2.12 illustrates the basic steps of the reconstruction code. The raw gated scans in Figure 2.12a are taken at varying source powers, to keep the count rate and afterpulsing constant. By simply scaling the intensity of each gated scan by the amount of source power attenuation used for that particular gate, the time-invariant portions of the gated signals match up while the transient, time-variant "bumps" do not. These bumps last for about 0.5 nanoseconds after the rising edge of the optical gate. They are actually distortions due to the sub-optimal biasing of the SPAD during the gate transition, which produces a time-variant response [46]. The time-variant response is cumbersome to model, since the instrument response must be taken for each increment of the need time resolution. Thus, it is crucial to take a large enough set delays to exclude the distortion, using the reconstruction code, to avoid modeling the time-variant portions of the response [46].
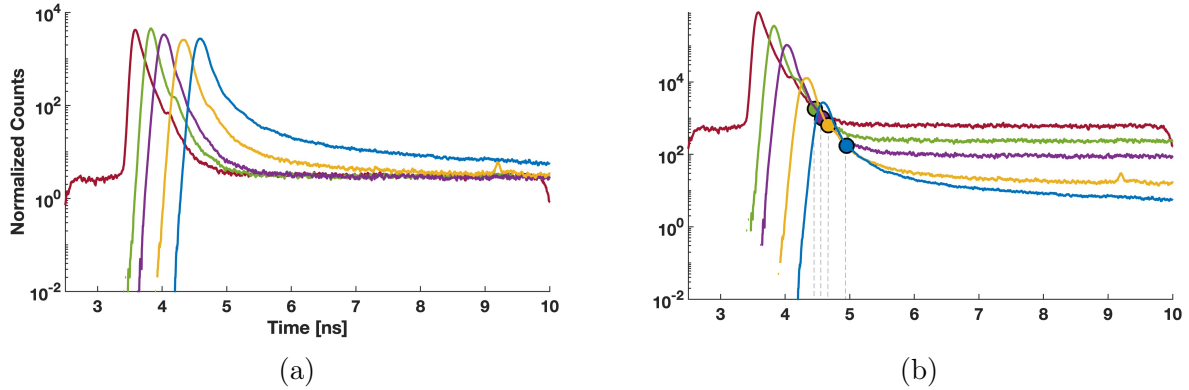
Figure 2.12: Individual gated scans are taken keeping the count rate constant. After loading the data, the intensity of each gate is scaled up by the amount of attenuation that was needed. The gated pulses are combined at the nearest point of overlap, show in Figure 2.12b (colored circles).

Once each gate is scaled, there is a nearest point of overlap between adjacent gates that needs to be found programatically. This crossover point is defined when the time-variant portion of the later gate just becomes time-invariant. To find this point programatically, a code was written that takes the absolute difference between adjacent gate signals. Then the minimum of the absolute difference is where the two signals are closest to each other in intensity. This point is where the adjacent signals are combined, which are shown as colored circles in Figure 2.12b. Figure 2.13b shows a fully reconstructed signal of combined gated signals (black line) compared to the ungated "free running" signal (magenta line) taken in a transmittance IRF configuration (Figure 2.13a).

2.4.3 Dynamic range and performance test

The first way to test the gated detector and TCSPC performance is by directly coupling the laser to the detector, to collect the transmittance IRF. A direct coupling of the laser to detector makes sure there is an excess of power, so that we can really test the dynamic range limits of the SPAD-TCSPC detector. Of course, it must be assumed that the beam was efficiently coupled to the SPAD and that the TCSPC counts were within the allowable range of $\leq 10\%$ of the sync rate.
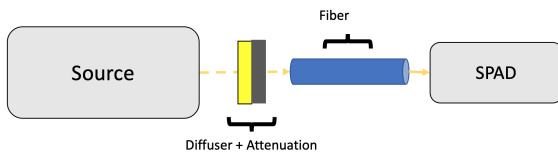
(a)
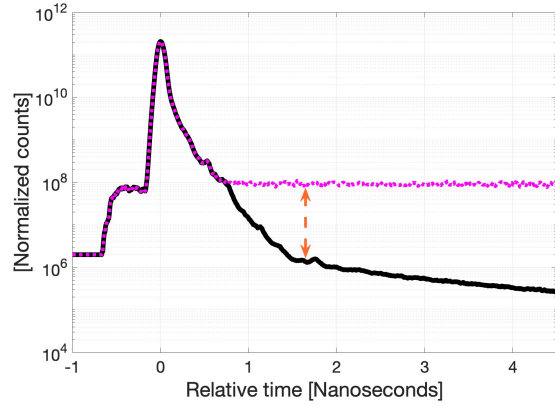
(b)

Figure 2.13: The black line shows the reconstructed IRF of the gated SPAD test. the Magenta dotted line shows the same IRF in "free running" mode. Figure 2.13a shows the configuration of a transmittance IRF test.

It is clear from Figure 2.13b that the noise level of the detector response is decreased by nearly two orders of magnitude after reconstruction. This is a tangible increase in performance already, just from using the gating technique. As we have seen from subsection 2.4.2, delaying the gate so that the rising edge comes after the earlier photons allows increasing the pulsed source power while maintaining the same count rate, and thus the background noise of the detector stays low.

Chapter 3

Phantom experiments

to test the accuracy of our DT and TRDRS methods, measurements on phantoms with calibrated optical properties were used to compare to the N-layer cylinder DT approximation of the RTE described in subsection 1.2.4. Calibrated phantoms can be made in either a solid-state or liquid form. The first test was on a solid state phantom fabricated with absorbers and scatterers mixed in a polymer suspension, because the phantom was already fabricated and easier to repeatedly measure.

In addition the phantoms tested here were designed to have two-layers with differing optical properties: a top layer of thickness 1-2 cm and a bottom layer approximating an infinite depth. The lateral boundaries were made to approximate infinity in each direction. Using a phantom with two layers is ideal for testing a time-gated system because depth sensitivity can be investigated. The purpose of time-gating is to increase the dynamic range and thus the depth sensitivity of the system, particularly for small SDS. So using a two-layer phantom and DT to see if the system can accurately resolve both layers would confirm the merit of using time-gating.

Solid phantoms have the advantage of structural integrity. If made properly, solid phantoms will also have no air bubbles and be homogeneous. The main drawback of solid phantoms is that they take more time to fabricate; and, once cured, the phantom optical properties cannot be adjusted.

3.1 Two-layer polymer (solid-state) phantom

A solid phantom, two-layer phantom shown in Figure 3.1 was made using a custom in-house fabricated polydimethylsiloxane (PDMS) polymer phantom as the top layer and a commercially manufactured polyurethane (PUR) phantom (INO, Canada) for the bottom. The PDMS layer used black drawing ink as an absorber and TiO_2 as a scatterer. Similarly the PUR phantom used black carbon as the absorber and TiO_2 as a scatterer.
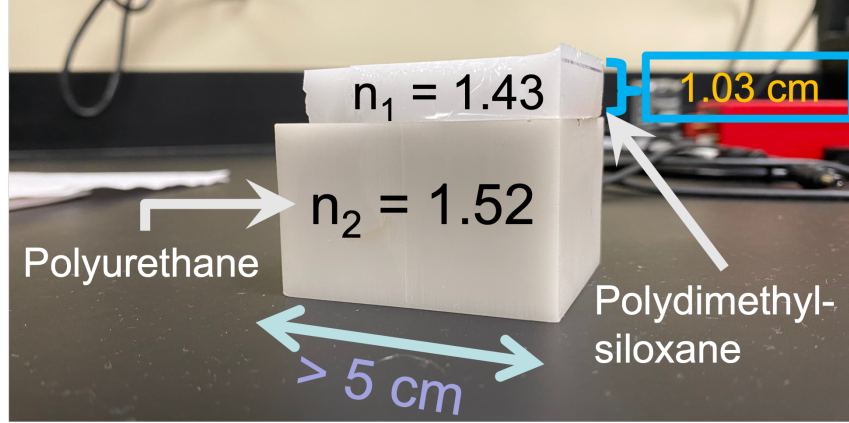
Figure 3.1: An image of the solid state layered made with a 1.03 cm thick slap of polydimethyl-siloxane and 3.47 cm thick block of polyurethane, the properties summarized in Table 3.1.

The PUR phantom properties were characterized by the manufacturers while the PDMS phantom was characterized using a time domain transmittance technique mentioned in sub-section 1.2.3. The recovered optical properties using the finite slab DT model are show in Figure 3.2b, along with Figure 3.2a, which shows the DT convolved transmittance fit-ted to the measured transmittance. All of the nominal optical properties of the solid slab based phantom, amalgamated from manufacturer data and finite slab TRDRS analysis, are summarized in Table 3.1.

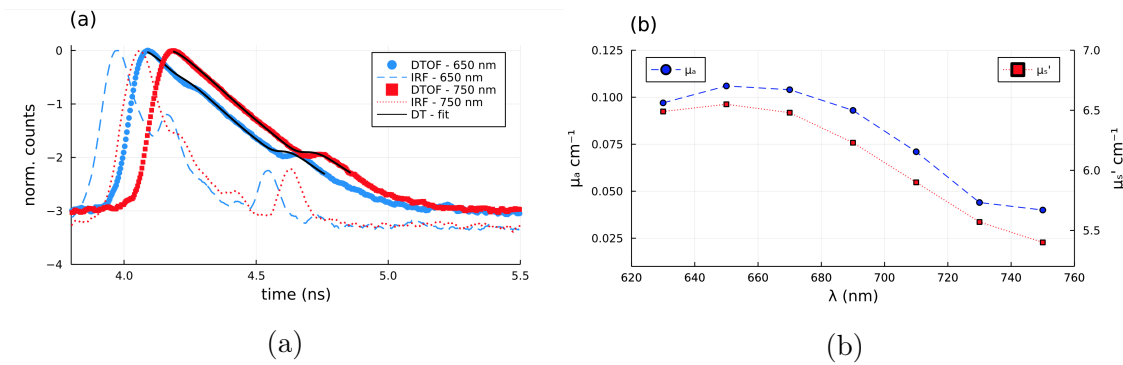Figure 3.2: Figure 3.2a shows the IRFs (dotted lines) and measured transmittance (symbols) for $\lambda = 650$ nm (blue) and $\lambda = 750$ nm (red). The black lines are the DT convolved transmittance for the recovered properties (i.e. the DT generated TPSF for the recovered properties convolved with the IRF). Figure 3.2b recovered absorption (blue symbols; left scale) and scattering (red symbols; right scale) coefficients.

Table 3.1: The nominal properties of the two-layer phantom shown in Figure 3.1. The PDMS layer was characterized by finite slab geometry DT fitting. The PUR layer properties were given by the manufacturer. The refractive index of PDMS was taken from literature reports.

	Layer 1	Layer 2
Material	PDMS	Polyurethane
Thickness	1.03 cm	3.47 cm
Refractive index	1.43	1.52
@ $\lambda = 650$ nm	$\mu_a = 0.105$ cm^{-1}	$\mu_a = 0.212$ cm^{-1}
	$\mu_s' = 6.55$ cm^{-1}=	$\mu_s' = 11.90$ cm^{-1}
@ $\lambda = 750$ nm	$\mu_a = 0.042$ cm^{-1}	$\mu_a = 0.183$ cm^{-1}
	$\mu_s' = 5.37$ cm^{-1}	$\mu_s' = 10.30$ cm^{-1}

Reflectance measurements of the entire layered solid phantom were taken at two source-detector separations–$\rho = 5$ mm and $\rho = 10$ mm–and wavelengths of $\lambda = 650$ nm and $\lambda = 750$ nm. The gated measurements were recombined into a single reconstructed time-resolved waveform using code written in MATLAB that was briefly described in subsection 2.4.2.

To interpret the data, the DT solution for a N-layered cylinder (subsection 1.2.4) geometry was computed as a forward model to be convolved with the IRF. Error between the measured and convolved reflectance was quantified and visualized.

3.2 Two-layer liquid phantom

Creating liquid phantoms provides more freedom in adjusting parameters of the sample such as the thickness of the top layer and the optical properties of each layer. This can be seen in Figure 3.3a where the open-lid container makes it straightforward to add more phantom solution to the top, increasing the volume and thus the thickness dimension of that layer. There is also a funnel for adding concentrated absorber to increase the absorption of the bottom layer. A 3D printed container composed of polylactic acid (PLA) was used to house the liquid phantoms that were used for further time-gated TRDRS studies (Figure 3.3).
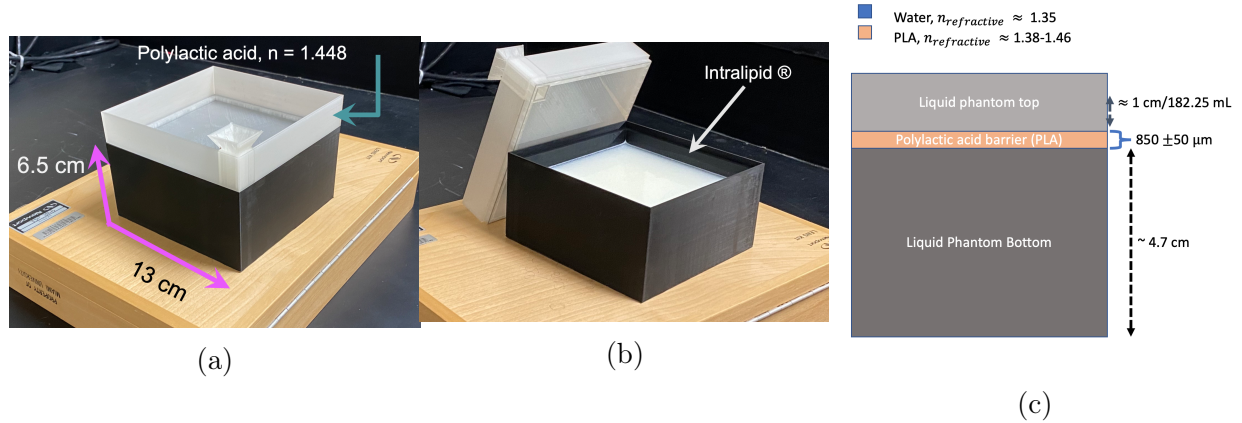
Figure 3.3: The phantom container was composed of PLA, with a literature refractive index value of 1.448. The length and width are 13 cm. Figure 3.3c shows a schematic of the cross section of the chamber. The inner volume height of the bottom chamber is about 4.7 cm, holding ∼800 mL of solution. The top and bottom chamber are separated by an opaque but translucent PLA lid of 850 ± 50 μm. The depth of the phantom in the top chamber is controlled by the volume, with 182.25 mL of volume correlating to 1 cm of depth.

3.2.1   Making calibrated phantoms

Liquid phantoms are mostly composed of deionized (DI) water, with carefully added concentrations of aborbers and scatterers. The liquid phantom calibration procedure used here involved a single absorber–dry bovine hemoglobin (Sigma-Aldrich, Missouri)–and a single scatterer–20% Intralipid (20% IL) solution (Fresenius Kabi, Germany).

A 1500 mL stock solution of the phantom was made with 500 mL having the optical properties of top layer and 1000 mL having those of the bottom layer. The bottom layer of the container shown in Figure 3.3b has a capacity of ≈860 mL when full with no air bubbles.

The bovine hemoglobin absorber was calibrated by first making an approximately 40 mg/mL of hemoglobin solution using DI water. This concentrated bovine stock solution was diluted into 5 separate volume concentrations spanning [0.01 0.1] mL stock per mL of total solution. A previously validated [18, 24] method of using a spectrophotometer to measure absorbance through a precisely 1 cm thick quartz cuvette as a function of volume concentration was used here. Figure 3.4 shows the results of these measurements for a particular batch of bovine stock solution at a wavelength of $\lambda = 785$ nm. It is noteworthy that the volume extinction coefficient (slope) varies significantly from batch to batch of hemoglobin and must be recalibrated every time a new stock absorber is made.
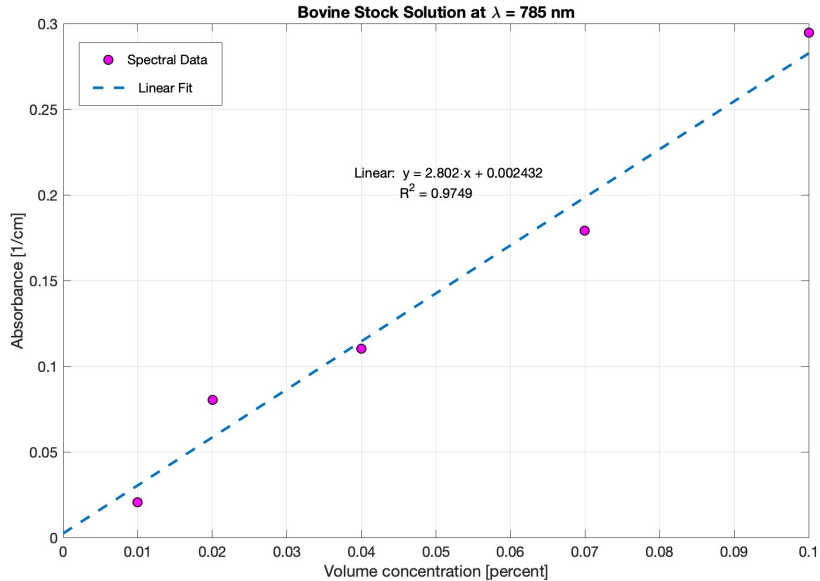
Figure 3.4: Calibration curve for a stock solution made of hemoglobin and DI water. μ_a vs volume concentration is plotted here with the slope of the linear fit being used as the volume extinction coefficient for absorption calibration.

The volume of IL20% added for calibration of the phantom stock solutions was computed using a well validated [47, 24] empirically derived formula. A 5% concentration of IL20% usually leads to the desired scattering properties over the spectrum of interest. Because medical grade IL20% is very reliable from batch to batch [48, 49, 50] using an empirical formulation is justifiable.

3.2.2 Analysis of phantom container

To test the DT model on the data, it was essential to get reference values for the optical properties, as well as the physical thickness of the PLA layer (see Figure 3.3c) that separated the top and bottom liquid layers. This would allow us to compare a two layer DT cylinder model (no lid) to a three layer DT cylinder, without making sweeping assumptions about the properties of the thin PLA lid. The physical thickness and optical properties of each layer are required as input parameters for the DT forward model.

The physical thickness of a phantom layer can be measured down to an accuracy of $\pm$ 0.05 mm using a Vernier scale caliper that was available in the lab. It was found that the physical thickness of PLA lid was 850 ± 50 μm (Figure 3.3c).

The optical properties namely refractive index, absorption coefficient and scattering co-

efficient were different story. The refractive index of PLA is available in the literature, but it can also be estimated in the lab. We decided to use an optical coherence tomography (OCT) instrument at $\lambda = 830$ nm wavelength to estimate the refractive index and also compare the result with the literature reports. For the absorption and scattering, there were no available reports in the literature, but we had a way to easily 3D print thin samples and use a single integrating sphere to estimate these optical properties [51]. The next two sections will describe in more detail the process of estimating the refractive index, absorption coefficient and scattering coefficient of the $3^{\rm rd}$ layer.

Optical coherence tomography measurements

Optical coherence tomography OCT is a method for acquiring cross-sectional images of a thin sample by measuring back-scattered light. A spectral OCT instrument developed at Miami University [52] was used to measure the optical pathlength of the sample directly from the Fourier transform of the spectral OCT image. A basic schematic of the instrument used for OCT scans is shown in Figure 3.5.
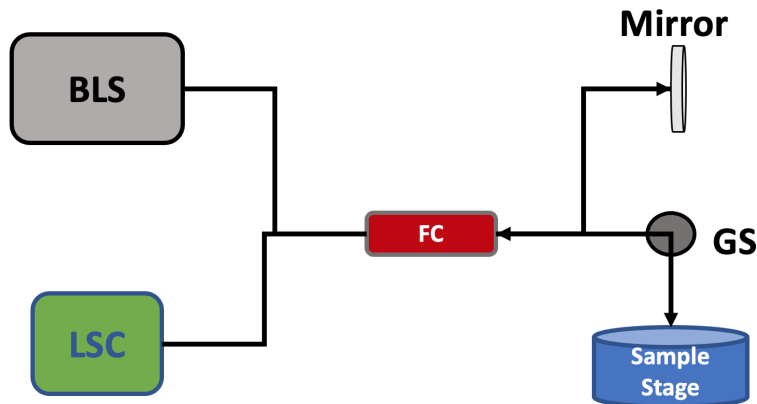
Figure 3.5: General schematic of the spectral OCT device used to measure the optical path length of the PLA sample. A broadband light source, BLS, is split 50/50 by a fiber coupler, FC. 50% of the transmission goes to the reference arm, consisting of a mirror, and the other 50% goes to the sample stage. The sample is imaged by a galvanometer scanner, GS, and artifacts from the image channel are corrected for using a separate GS. Diffuse backscattered light from the sample is sent to a line scanning camera, LSC, and interferometric signals between the sample and the reference channel are detected spectrally.

In spectral OCT, broadband interference is measured using an array of detectors or a camera after passing through an appropriate grating for spectral dispersion. The device used here was powered by a 200 MHz supercontinuum light source (YSL, Wuhan City, China) and filtered at a central wavelength of $\sim$830 nm and a bandwidth of $\sim$150 nm FWHM. The light was coupled into a fiber coupler, FC, that split the input power 50/50 to the reference and sample arm. The sample arm collimated the light into a beam and scanned the sample using two galvanometer scanning mirrors. Back-scattering light from the sample was steered by the FC back to the 4th channel, sending the beam through a grating and focusing it into a line scanning camera, LSC. Interference with the reference beam reflected by the reference mirror is what was measured.

By definition, the optical path length is the product of the refractive index and the geometric length for a homogeneous medium. The geometric length is just what we have been calling the physical thickness of the sample. The optical path length can be measured directly from the Fourier transform of the spectral OCT image. Knowing these two lengths, the refractive index, n, can be estimated by

$$n = o/l,$$

where o is the optical path length and l is the geometric length. The Fourier transform can be practically implemented using a fast Fourier transform (FFT) algorithm.
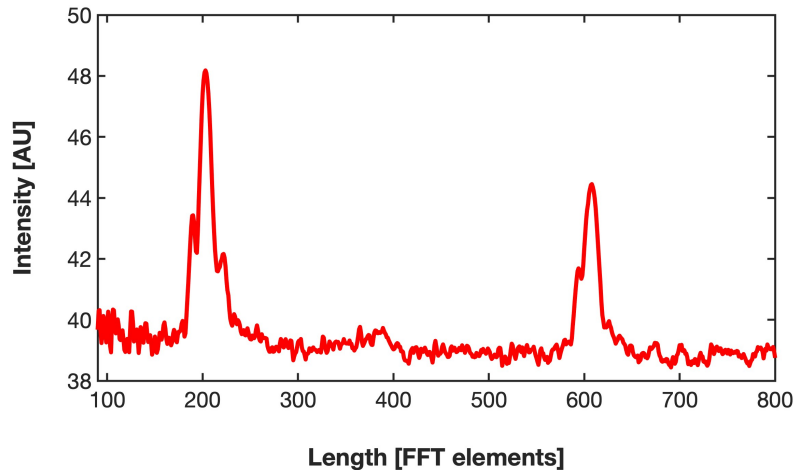

Figure 3.6: Shown is the spectral OCT image after a fast Fourier transform. The peaks represent reflections and the distance between them is the optical thickness. The thickness was scanned laterally for 1.2 mm so for this figure an average optical thickness is displayed.

Figure 3.6 shows the result of a FFT on the measured spectral OCT image averaged laterally over the image. The x-axis is the length dimension, in units of FFT elements. The two peaks are reflections representing the boundaries of the sample.

The particular sample cross section image shown in Figure 3.6 is that of a 175 ± 5 μm thick NBK-7 glass microscope slide. This measurement was taken as a reference for the amount of micrometer length units there were per FFT element unit. Once this conversion was estimated, a 3D printed PLA sample of 250 ± 50 μm thick was imaged and the measured optical thickness from the FFT image was converted to micrometers. The PLA refractive index was estimated by $n = o/l$ and was found to have an expected value of 1.34, with a very high sensitivity to relatively large uncertainties geometric length. In other words, the estimated refractive index could change to 2.7 by slightly decreasing the geometric length input. An even thicker sample was printed, of 2000 μm to decrease the sensitivity, and still an expected value of 1.34-1.36 was estimated using the 2000 μm as the geometric length input, with still a high sensitivity to length uncertainty.

Integrating sphere

A method for characterizing the $\mu_s{}'$ and μ_a of a thin sample is to use a single integrating sphere and inverse adding-doubling algorithm (IAD). This method is well described elsewhere [51] and was set up in the lab accordingly. Two 3D-printed PLA samples were measured for and used as inputs for the algorithm, one of thickness 850 μm and the other of 2000 μm. The IAD recovered properties are summarized below in Table 3.2.

Table 3.2: The estimated optical properties of the PLA layer using an integrating sphere and IAD algorithm.

Sample Thickness (μm)	λ (nm)	$\mu_s{}'$ (cm^{-1})	μ_a (cm^{-1})
850	650	3.42	0.49
850	750	3.57	0.60
2000	650	5.61	0.49
2000	750	5.53	0.51

3.2.3 Set of measurements

In the following chapter we will discuss the results of layered phantom experiments. Moving from the solid layered phantom to the liquid one, the first parameter we chose to vary was

the thickness of the top layer. Table 3.3 summarizes the new measurements that were take on the liquid phantom testing Layer 1, L_1, thickness.

Table 3.3: The set of measurements acquired on the two-layer liquid phantom designed in subsection 3.2.1. L_1 stands for "Layer 1". All measurements were taken in the reflectance geometry with the probe facing the phantom from top layer to bottom layer.

Measurement	L_1 Thickness (mm)	SDS (mm)	Wavelength (nm)
1	10	5	650
2	10	5	750
3	10	10	650
4	10	10	750
5	15	5	650
6	15	5	750
7	15	10	650
8	15	10	750
9	20	5	650
10	20	5	750
11	20	10	650
12	20	10	750

Previous have shown that time gated TRDRS can improve the detection or sensing of small inhomogenieties at depth [23, 53]. Additionally, studies have investigated multiple layer systems [27, 25] to recover layer thickness or optical property estimates. However, the none of the studies using gating use DT or Monte Carlo simulations to estimate optical properties. Further, the layered phantom studies either use continuous wave diffuse optical spectroscopy or nongated time resolved spectroscopy. None of the studies to our knowledge test layer phantoms using a gated TRDRS system and the N-layered cylinder DT solution in the time domain.

The question was if the gated method had advantages over the ungated method for resolving multiple layers with the N-layer cylinder DT model? The measurements were designed to give us data that could help us answer this question.

Chapter 4

Analysis of experimental data

Testing the newly built time-gated TRDRS system against the standard nongated TRDRS system was a major aim of this research. Another desirable result is to try to quantify the properties of the sample and check the accuracy of the estimations. The superior depth sensitivity of gated TRDRS is validated and quantified in terms DTOF moments, which are measures of the shape of the distribution.

4.1 Sensitivity analysis

With the 3D printed container and calibrated liquid phantoms, there are more free parameters that can be varied experimentally. The focus of the liquid phantom study here was specifically to change one parameter, the thickness of the upper layer. The effect of varying layer thickness was tested and compared using gated and ungated TRDRS.

4.1.1 Boundary effects

Before making calibrated phantoms, inexpensive phantoms made out of whole (3.5% fat) milk to test the boundary effects of the phantom container. A 3:1 ratio of whole milk to DI water should produce tissue-mimicking scattering properties [35].

The data in Figure 4.1 shows the diffuse reflectance when bottom of the phantom chamber was filled with the scattering solution, imitating a homogeneous semi-infinite medium. The measurement was repeated for an SDS of $\rho = 5$, 10 and 15 mm at a wavelength of $\lambda = 650$ nm. The PLA lid of of the container was placed on top and the same scans were taken (shown as red line).

The depth of the scattering solution in the bottom layer of the container, was between 4 cm to 5 cm. In addition, the radial distance from the source to the lateral boundaries of the container was over 5 cm.

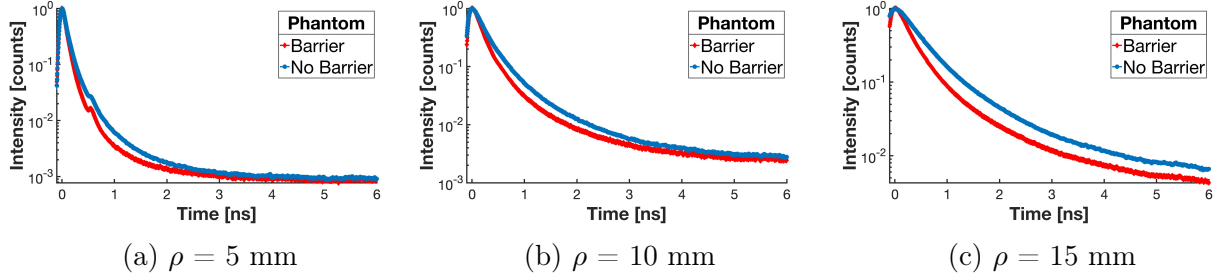(a) $\rho = 5$ mm　　　　　(b) $\rho = 10$ mm　　　　　(c) $\rho = 15$ mm

Figure 4.1: The measured reflectance of an effectively semi-infinite milk phantom (blue diamonds line) and the reflectance of the same phantom with the 850 μm PLA layer (see Figure 3.3c) on top. The reflectance with the PLA barrier present shows a significant perturbation as compared to no barrier being present.

It is clear that the presence of the PLA lid perturbs the shape of the DTOF significantly. The red line has a greater decay slope, which is consistent with the affect of absorption. Our integrating sphere analysis of the PLA lid indicated that the PLA does have a relatively high estimated absorption coefficient of 0.4932 cm^{-1} at $\lambda = 650$.

The ideal lid between two liquid layers of a phantom is one that makes no noticeable disturbance to the DTOF. In order for this to be the case, the lid must be very thin, around 50 μm and have a slight amount of scattering (translucence) to wash out the refractive index mismatching [54]. Since our lid made of PLA clearly does impact the DTOF drastically, one might suppose that a three layer cylinder DT approximation would be superior to the two layer model.

To test the effect of the bottom of the boundary of the container and avoid these potential boundary effects, the bottom was filled with the homogeneous milk phantom to a depth of 4 $\pm$ 0.05 cm followed by 5 $\pm$ 0.05 cm and scanned. Figure 4.2 shows that there were no effects due to the bottom boundary of the container at these depths.

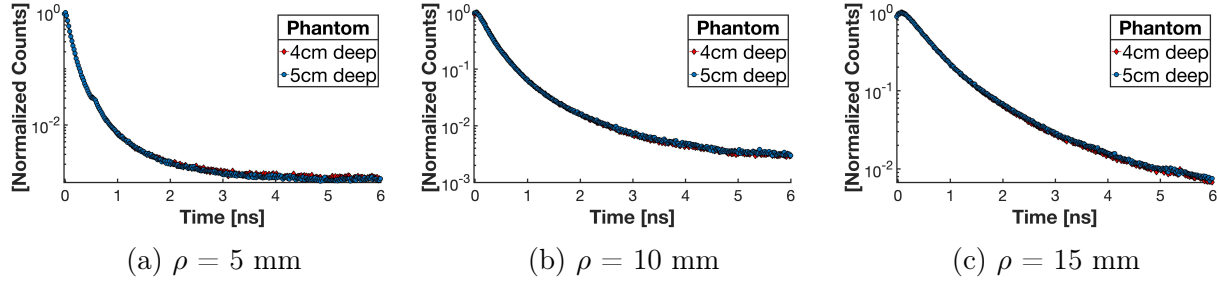(a) $\rho = 5$ mm (b) $\rho = 10$ mm (c) $\rho = 15$ mm

Figure 4.2: The DTOF at increasing SDS' when the homogenous milk phantom filled the bottom of the chamber to a depth of 4 ± 0.005 cm (red line) and 5 ± 0.005 cm (blue line).

Even at the largest SDS of 15 mm, which corresponds so more depth sensitivity, the DTOF was stable between adjusting the depth from 4 cm to 5 cm. This means that as long as we fill up the bottom chamber, which holds inner volume of 860 mL with a height of 4.7 cm, we will be safe from any boundary effects to the bottom of the liquid phantom container.

4.1.2   Top-layer thickness

The calibrated phantoms of bovine hemoglobin and 20% IL were made to test the effect of varying the top layer thickness. Phantoms were designed according to the procedures in subsection 3.2.1 to make phantoms with the optical properties summarized in the table below. Table 4.1 summarizes the expected optical properties of each layer of the liquid phantoms, including the PLA lid.

Table 4.1: The nominal optical properties of the calibrated phantoms and PLA lid. The absorber calibration was based on spectrophotometry and scatterer from cross validated empirical formulations. The PLA properties were from OCT and integrating sphere with IAD techniques.

Layer	wavelength (nm)	μ_a cm^{-1}	μ_s' cm^{-1}	refractive index
Layer 1	650	0.138	13.16	1.35
PLA lid	650	0.4932	3.424	1.34-1.46
Layer 2	650	0.195	13.16	1.35
Layer 1	750	0.107	11.00	1.35
PLA lid	750	0.6027	3.569	1.34-1.46
Layer 2	750	0.152	11.00	1.35

Reflectance measurements of the phantoms with three separate Layer 1 thickness levels were taken for wavelengths $\lambda = 650$ nm and $\lambda = 750$ nm and SDS $\rho = 5$ mm and 10 mm. The thickness of to upper layer was changed from 10 mm to 15 mm to 20 mm by increasing the

43

volume of the liquid phantom in the upper layer in increments of ~180 mL. Actual thickness was measured using a Vernier scale ruler with a tolerance of ± 0.05 mm.

(a) $\lambda = 650$ nm Gated

(b) $\lambda = 650$ nm Ungated

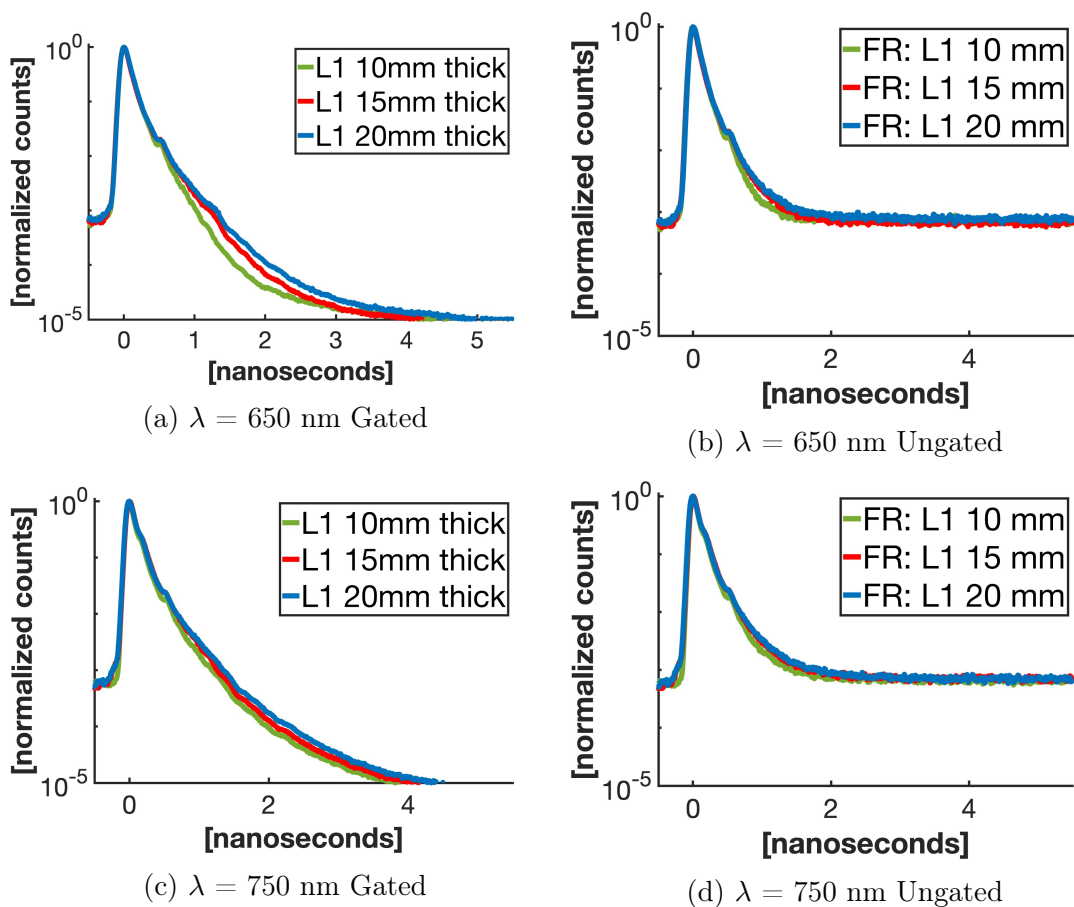(c) $\lambda = 750$ nm Gated

(d) $\lambda = 750$ nm Ungated

Figure 4.3: Figure 4.3a shows the DTOF of the liquid phantom for an upper layer thickness of 10 mm, 15 mm and 20 mm acquired at a wavelength of 650 nm and SDS of 5 mm. Figure 4.3c shows the DTOF for the same phantoms but with a wavelength of 750 nm and SDS 5 mm. The gated and ungated methods are compared visually.

The data in Figure 4.3 shows that the shape of the DTOF at later times is perturbed by thickness changes of the top layer in the gated regime. For both $\lambda = 650$ nm and $\lambda = 750$ nm, the ungated DTOF does not show significant change in shape as the thickness is changed. In contrast, the gated DTOF shows a visible increase in the slope of the tail as the thickness of layer 1 decreases. This indicates that time-gated acquisition allows for sensing the change in optical properties from top to bottom layer of the liquid phantom whereas the ungated mode cannot. This result opens up the question of whether the gated DTOF can be used to retrieve the optical properties of the bottom layer.

4.2   Diffusion theory on phantom data

A standard way to retrieve optical properties is to fit the DTOF using the diffusion approximation described in section 1.2. The first test was to input the expected optical properties into the diffusion theory model and see how well the data match or deviate from the theoretical expectation.

4.2.1   Two-layer polymer phantom

The solid phantom described in section 3.1 was measured as a preliminary test of the layered cylinder DT model. There were two wavelengths and two SDS' used for a total of four unique reconstructed signals. Signals were reconstructed using a MATLAB code described in subsection 2.4.2 and each IRF and DTOF required 4-5 gated acquisitions.

Figure 4.4 shows a plot of each SDS-wavelength combination that was reconstructed. An IRF that was convolved with the DT model with the nominal input parameters is include as a gray dashed line. The black dots are the actual measured DTOFs that should in theory match with the DT forward model (red dashes) with the correct input parameters.

(a) SDS = 5 mm, $\lambda = 650$ nm
(b) SDS = 10 mm, $\lambda = 650$ nm
(c) SDS = 5 mm, $\lambda = 750$ nm
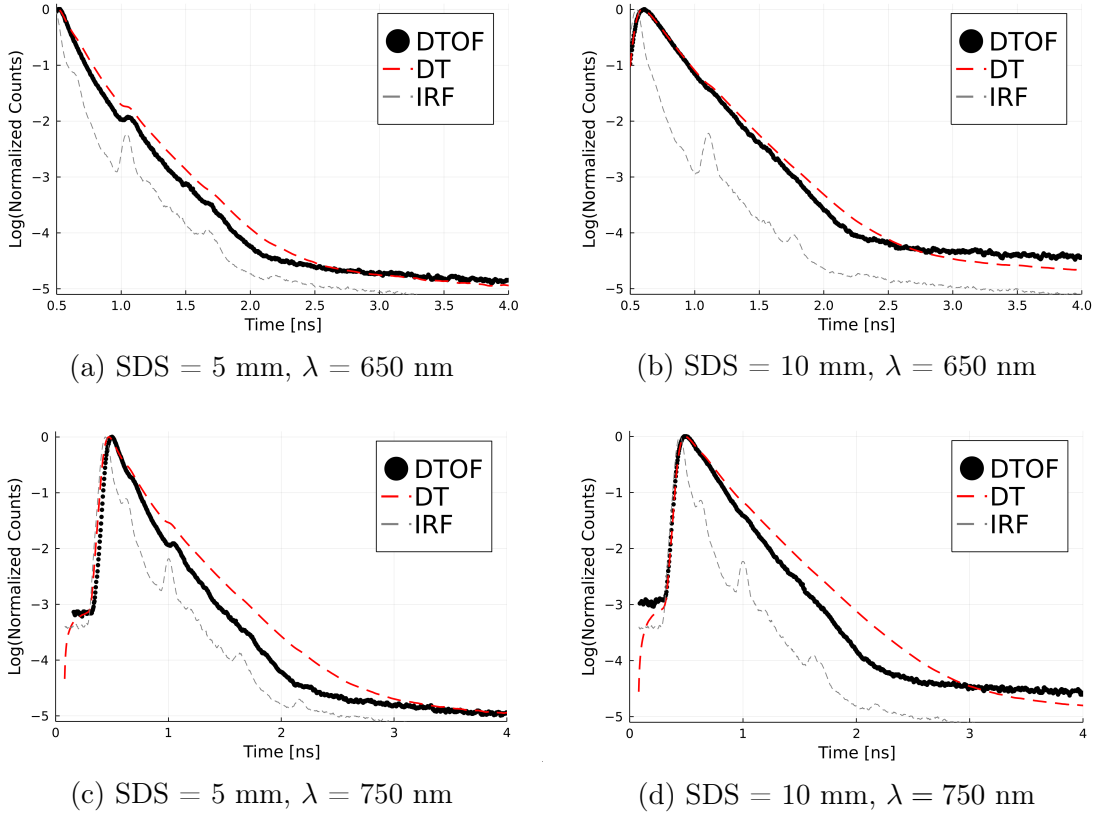(d) SDS = 10 mm, $\lambda = 750$ nm

Figure 4.4: The forward DT model convolved reflectance (red dashes) are plotted with measured reflectance (black dots). The gray dashed line shows the IRF that was used for convolution with the DT temporal point spread function.

The reflectance is plotted on a logarithmic scale, which means that visually the error between the theoretical and the measured reflectance is hard to analyze. From Figure 4.4, it appears that the model matches the measurements well at early times and deviates only at the later times.

When trying to solve the inverse problem through nonlinear regression, such as using a standard Levenberg-Marquardt (LM) algorithm, it is crucial that the errors are minimized when the correct parameters are put into the model.

Residuals

The residuals, or the difference between the measured and expected values, as a function of time are what needs to be optimized when inverse fitting. To get an idea of how accurately the inverse model may predict the nominal optical properties, the residuals were computed

46

as a function of time for the preliminary solid phantom data. They are computed straight forwardly by taking the measurement value at a each time value and subtracting the expected value at that time:

$$\text{residual}(t) = \text{measured}(t) - \text{expected}(t)$$
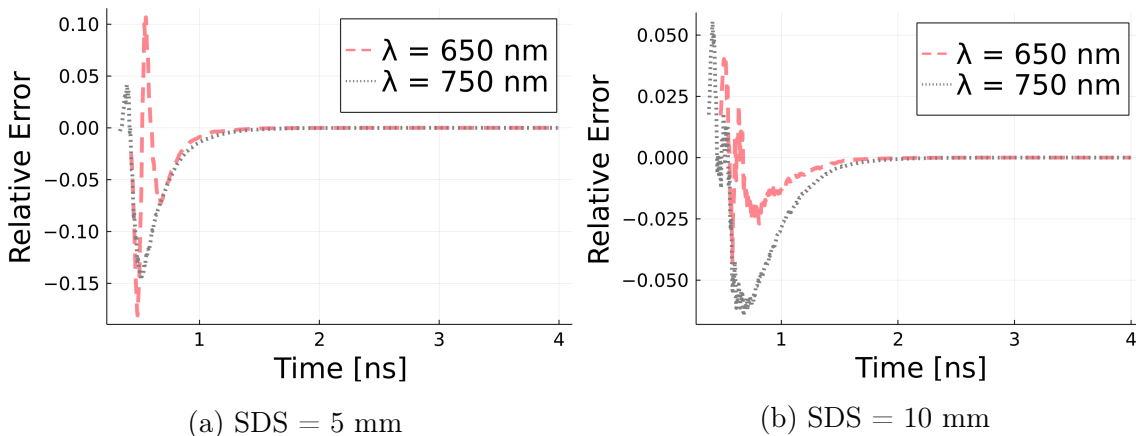

(a) SDS = 5 mm　　　　　　　(b) SDS = 10 mm

Figure 4.5: The residual between measured reflectance and two-layer DT reflectance are plotted for each SDS. For each SDS residuals for $\lambda = 650$ (red dashes) and $\lambda = 750$ (gray dashes) are shown.

In Figure 4.5, the y-axis is relative error ranging from [0,1] because the reflectance is normalized according to the maximum count value before convolution.

The aspect of being on a logarithmic intensity scale makes it hard to resolve errors at the later times, where the counts are orders of magnitude less than the maximimum. This can easily be seen in Figure 4.5 where the residuals quickly decay to almost zero. This makes inverse fitting and LM algorithms highly sensitive to time window selected for fitting [55, 56]. As such, it may be best to avoid inverse fitting a leave the fit window as a topic of further research.

Residuals over the entire time window at $\lambda = 750$ nm appear to be greater overall compared to $\lambda = 650$ nm. This may be because of the lower SPAD efficiency at this wavelength along with a nonoptimal ZC level setting on the TCPSC system parameters. These would mean that the SPAD was not counting enough of the photons that hit it and bringing the ZC closer to baseline may serve to ease this issue.

4.2.2 Liquid phantom: two-layer DT model

Figure 4.6 shows plots of the measured DTOF and convolved DT DTOF in the same form as Figure 4.4 for the solid phantom but with a plot for each Layer 1 thickness used for the phantom. The DTOFs shown are at a wavelength of $\lambda = 650$ nm. The plots on the top row are for measurements taken at an SDS, $\rho = 10$ mm. The bottom row is for the SDS of $\rho = 5$ mm. Going from left to right, plots show data on phantoms with Layer 1 thickness from 10 mm to 15 mm to 20 mm.
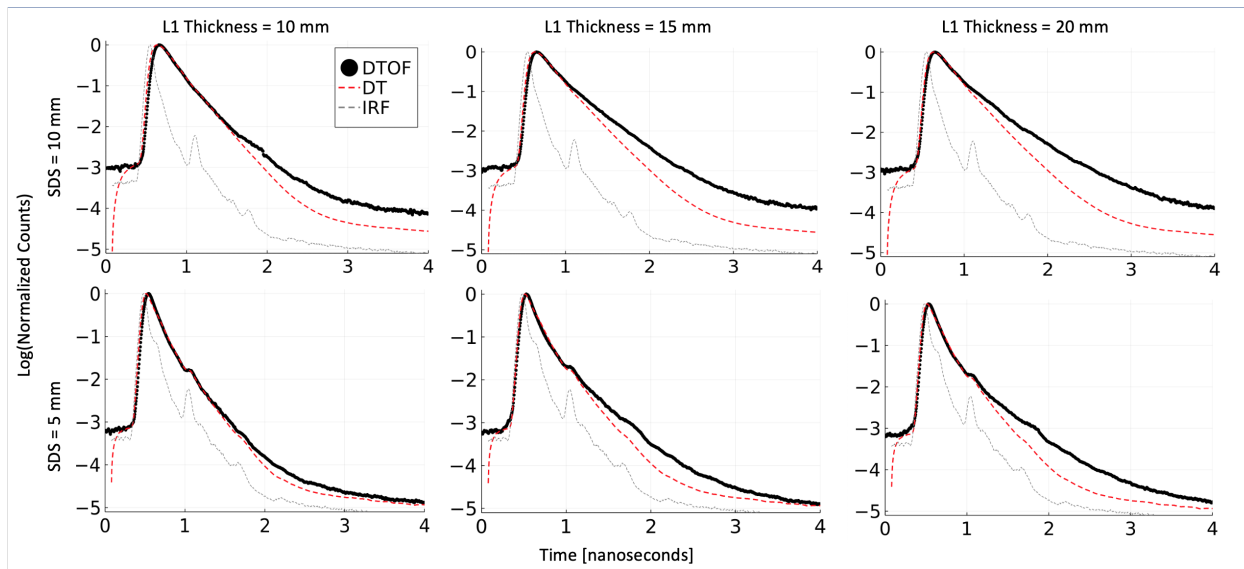

Figure 4.6: The raw DTOF (black circles), IRF (gray dashes) and two-layer DT forward model. The data is visualized raw through plotting each scan for the wavelength of 650 nm. From left to right, the thickness of the upper layer on the phantom increases from 10 mm to 20 mm. The first row represents scans taken at an SDS of 10 mm and the second $\rho = 5$ mm.

As with the solid phantom DT matching, there was an arbitrary time shift needed to compare the shape of the DTOFs because the TCSPC time scale of the IRF and DTOF were slightly different due to the experimental set-up for measurements. When inverse-fitting for optical properties, this time-scale shift should not be considered lightly [55, 56, 57], as an error in as little as 50 picoseconds can lead to an error in $\mu_s{}'$ on the order of 1 cm^{-1} [17]. However, for initial evaluation of the shape of the theoretical and experimental DTOFs here we "eyeball" the time scale so that they approximately match.

The deviation from DT at $\rho = 10$ mm clearly gets pronounced in the later arrival times, possibly due to the interface between the PLA and aqueous phantom. Additionally, the deviation appears to increase as the thickness of the top layer increases and begins to take

place at earlier arrival times. From the sensitivity analysis section, we saw that the measured DTOF was perturbed significantly with changes in phantom thickness of the top layer, however from DT analysis our two-layer phantom model shows shape changes on a much smaller scale.

Similarly for $\rho = 5$ mm, the deviation becomes more pronounced earlier on in the DTOF as the thickness of layer 1 increases. Overall, the measured DTOFs match the DT convolved DTOFs better for the SDS of $\rho = 5$ mm than for that of $\rho = 10$ mm.

The results seem to point to the effect of the PLA lid because of the devations at later times. It is possible that there where issues with an the air bubble under the lid, which was masked by the scattering phantom on top and that grew over time. There was slow but noticeable leaking of the phantom from the bottom chamber through the crease between the lid and bottom chamber that came in response to adding more liquid to the top. This could explain why the nonideal deviations got worse as the thickness was increased.

Without rebuilding the flawed container, we still had the option to test the three layer DT solution to see how much that would help. If adding a PLA layer with the appropriate properties significantly improved fits, that itself would be an important finding.

4.2.3   Liquid phantom: three-layer DT model

Because the container itself had a barrier of finite thickness separating the top and bottom aqueous phantom solutions, there was a reason to suppose that trying to model it with a three-layer DT model would improve the fits. To find out, the DT solution for a three layer cylinder was computed and convolved with the IRF.

It was easy to program another layer into our model because the DT solution is for N number of layers. We simply added another layer with the 2nd layer having the properties of PLA while the 1st and 3rd layers maintained the liquid phantom properties used in the two layer model.
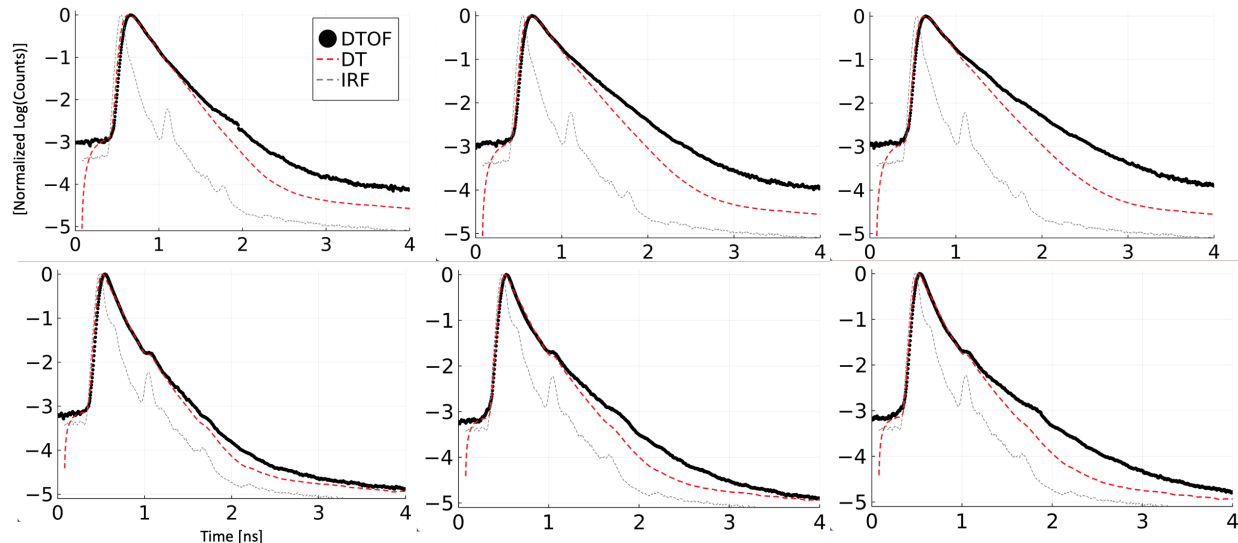
Figure 4.7: On each of the axes, the DT three-layer model, measured reflectance and IRF are plotted for $\lambda = 650$ nm. From left to right, the top layer thickness of the phantom measured increases from 10 mm to 15 mm to 20 mm. The 1st row of plots were measured at an SDS of $\rho = 10$ mm and the 2nd row of $\rho = 5$ mm.

Unfortunately, after matching up the time scale and evaluating the shapes of the DTOF, the deviations were not noticeably improved as illustrated by Figure 4.7. This may be due to effects around the PLA boundary that are not easily modeled. For example it is possible the bovine hemoglobin absorber aggregated near the barrier at the bottom of the first layer due to not enough stirring, creating an effectively inhomogenous sample. It is also possible that due the the refractive index mismatch, low scattering and low physical thickness of the PLA barrier that there were light-guiding effects that cannot be described by our model [54]. Still, it is even possible there was an air bubble that slowly grew due to the design flaw of the container.

Residuals

comparing the residuals between two layer and the three layer DT fits will quantitatively show us if there was any improvement. In Figure 4.8 the residuals of the measured reflectance to the DT for the two and three layer models are shown as seperate lines on each plot. Only the residuals for the wavelength $\lambda = 650$ nm are shown (Figure 4.8) for simplicity.
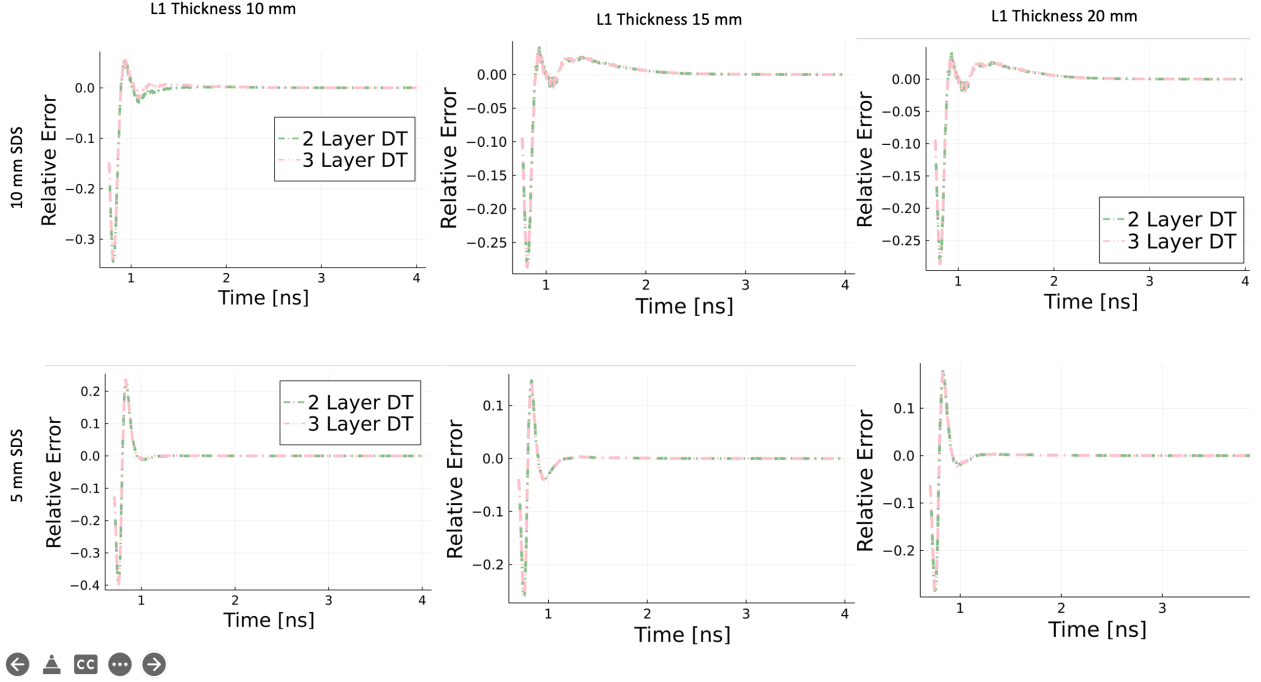
Figure 4.8: The residuals of measured reflectance to two layer DT (green dashed line) and three layer DT (pink dashed line) for the wavelength $\lambda = 650$ nm. From left to right, the top layer thickness of the phantom measured increases from 10 mm to 15 mm to 20 mm. The 1st row of plots were measured at an SDS of $\rho = 10$ mm and the 2nd row of $\rho = 5$ mm.

From these findings, it may be ideal to use caution when fitting for optical properties on the liquid layered phantom. Better results may be obtained when fitting the phantom with the least top-layer thickness or the solid phantom with effectively no 2nd layer and by using an approach to constrain the scattering coefficient [18, 56].

Summary of forward model errors

To summarize, errors between DT and experiment for each phantom tested were computed in χ^2 form,

$$\chi^2 = \sum_{j=1}^{k} \frac{(O_j - E_j)^2}{E_j},$$

where j in this case is the particular time bin, O_j is the jth observed (measured) count and E_j is the expected count for the jth time bin. Figure 4.9 shows the χ^2 statistic for the solid phantom experiments and liquid phantom experiments for both models. The χ^2 was average over each wavelength and each thickness of Layer 1 and compared by SDS.
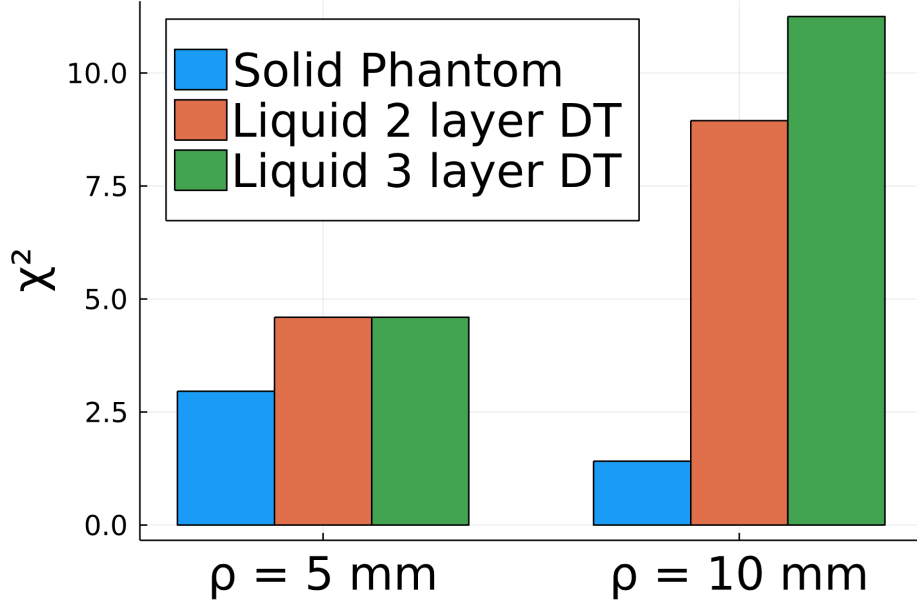
Figure 4.9: The errors computed in χ^2 form across each specific phantom measurement. The blue bar represents solid phantom, orange liquid phantom to two layer DT and blue the liquid phantom to three layer DT. Errors were averaged over wavelengths used and thickness of the Layer 1 if applicable.

In conclusion, the solid phantom fits were significantly better as compared to the fits of the layered liquid phantom (the lower the χ^2, the better). The change between using a two layer vs three layer DT model was unexpectedly minimal, indicating that there is something deeper going on leading to errors. Design flaws in the chamber are the most likely culprit of these errors and possibly the error is compounded by suboptimal TCSPC parameters.

4.3 Moments analysis

Another approach to characterizing a phantom using the measured DTOF is to completely avoid errors in timescale and crosstalk associated with $\mu_s{}'$, by strictly quantifying moments of the time-of-flight distribution and subtracting away the IRF effects [19]. Because our system clearly has some sensitivity to the depth of the layers but proved to not match with DT straightforwardly, we decided to focus our efforts on quantifying the moments of the measured DTOFs and relative differences after subtraction. Maybe the changes in the moments of the measured DTOFs will be useful in characterizing the phantom despite the mismatch with DT convolved DTOFs. It is conceivable that subtraction methods could help

eliminate errors caused by the phantom chamber as well.

Figure 4.10 shows the computed 1$^\text{st}$ and 2$^\text{nd}$ central moments. These moments correspond to the mean photon arrival time and the variance about the mean respectively.

(a) $\rho = 10$ mm

(b) $\rho = 10$ mm

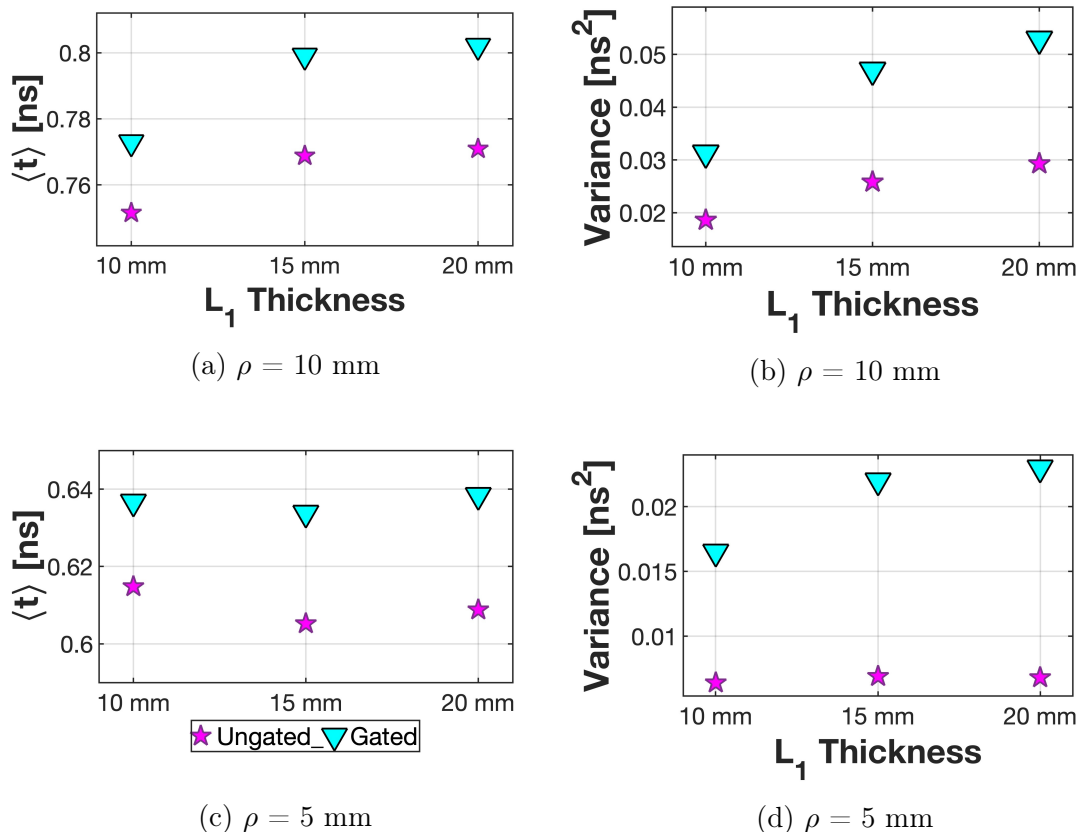(c) $\rho = 5$ mm

(d) $\rho = 5$ mm

Figure 4.10: Figure 4.10a shows the 1$^\text{st}$ normalized moment (mean arrival time) for the ungated regime (magenta stars) and gated regime (cyan triangles) at $\lambda = 650$ and $\rho = 10$ mm. Figure 4.10b show the same for the 2$^\text{nd}$ centralized moment, the variance in arrival time $V = \langle (t - \langle t \rangle)^2 \rangle$. On the bottom row Figure 4.10c and Figure 4.10d show the moments at $\lambda = 650$ for $\rho = 5$ mm.

The moments of gated and ungated DTOFs are clearly distinct from each other. The additional dynamic range of the gated DTOF significantly increased the 1$^\text{st}$ and 2$^\text{nd}$ moments by resolving significantly more late photons. This means that gating not only shifts the mean arrival time to a later time, but it actually also increases the spread of arrival times about the mean as compared to ungated detection.

The change in moments due to the change in layer 1 thickness (x-axis of plots) seems to be the approximately the same for the $\rho = 10$ mm (Figure 4.10a and 4.10b), which would indicate that both the ungated a gated acquisition modes are equally sensitive to changes in

thickness for $\rho = 10$ mm. For the case of $\rho = 5$ mm, there is definitely an improvement in sensitivity to thickness using gated (see Figure 4.10d) as shown by the change in Variance with thickness. The change in the mean arrival time $\rho = 5$ mm remains practically unchanged for both gated and ungated modes, which makes because it is well known that the 1st central moment is primarily sensitive to in the superficial layers of the sample while the 2nd is more sensitive to a few centimeters deeper in scattering media [10].

4.3.1 Moments subtraction

The moments of gated and ungated measurements proved to be significantly different (Figure 4.10), so the question is how does this impact the $\mu_s{'}$ estimates based on Equation 1.11? Although it was a struggle to use DT to model the DTOFs from the liquid layered phantoms, it is still possible to estimated useful information. Most notably, we could try to quantify $\mu_s{'}$ using the subtraction method of moments [19], especially because we made the liquid layered phantoms such that the scattering was the same in the top and bottom.
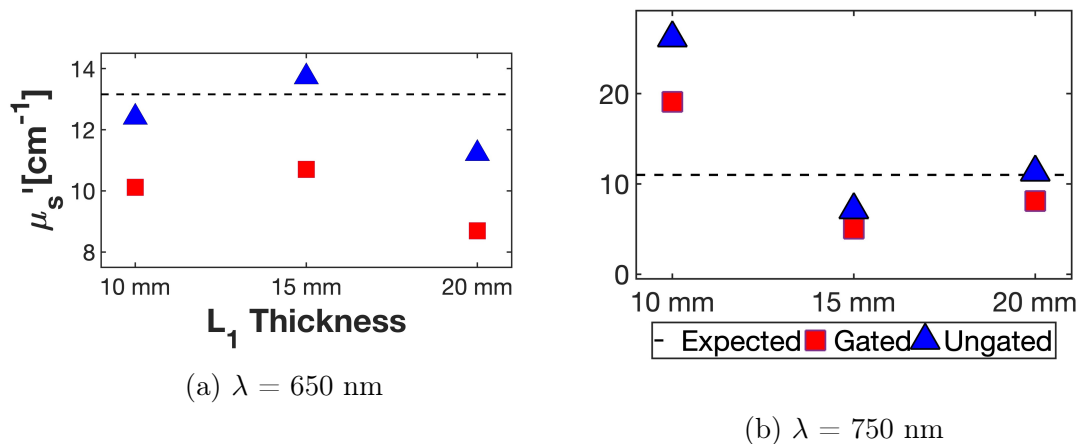
(a) $\lambda = 650$ nm

(b) $\lambda = 750$ nm

Figure 4.11: The dashed line are the expected optical properties and the symbols are estimates. The left plot is 650 nm and the right is 750 nm as a function of layer thickness

in Figure 4.11 the subtraction method introduced in section 1.3 was used to heuristically get a $\mu_s{'}$ estimate based upon the change in the 1st and 2nd moment across two SDS. The estimated were compared to the expected $\mu_s{'}$ from calibration.

Both ungated a gated moment differences produce reasonable estimates, with neither one performing better. If anything, the ungated DTOFs provided better estimates for the wavelength $\lambda = 650$ nm. However, it is stressed again that the time window matters significantly

as the time window chosen to compute the moments can be affected by noise level intricately [35]. For the computation of moments for these data, the ungated window went from 5% of the peak intensity on both the lower and upper limits. For the gated moments, the upper time limit was adjusted due to the increased resolution of late photons. Since the for an SDS of $\rho = 5$ mm, gating improves the noise level by around 80 times (or $\sim$1.9 decades), the upper time limit was divided by 80 to compute the moments over a time window of 5% to 0.0625% of peak intensity. The same process was follow for the SDS $\rho = 10$ mm, but the upper time limit was divided by 10 for the amount of noise level improvement from gating.

Conclusion & summary

In this thesis, the limits of time-gated TRDRS sensitivity were tested. Sources of error from phantom design and layered DT modeling were considered. Finally, possible methods for working around errors by using the moments of the DTOFs were studied.

We developed a functional time-gated TRDRS system and a 3D printed container to house two separate layers of calibrated liquid phantoms. The container allowed for freely varying the parameter of top layer thickness by increasing the volume of the top liquid layer. An experiment was designed in which the top and bottom liquid layers had the same μ_s' property and two different μ_a properties. The thickness of the top layer was varied from 10 mm, to 15 mm and to 20 mm while reflectance was collected using two seperate SDS and wavelengths in the gated and ungated regimes. As shown in Figure 4.3, decreasing the noise level using time-gating clearly helped improve the sensitivity of TRDRS at the later arrival times where there are less photon counts.

The measured data on the liquid phantoms housed in the 3D printed container and also on a two layer solid slab phantom could be simulated using the layered DT model (subsection 1.2.4). The expected optical properties for each layer of each phantom were estimated using well validated techniques before using those expected values as input parameters for the DT forward model. The DT and measurement time shifts were matched through "eyeballing" and the DTOF shapes were compared. Deviations from the theoretically expected DTOF were analyzed by taking residuals and using the χ^2 goodness-of-fit statistic. It was found that the residuals and hence the χ^2 errors were very heavily weighted towards the early photon arrival times, leading to a high sensitivity to error based on the fitting window selected and the knowledge of "true" time zero. Additionally, there was an increased error in the liquid phantom measurements at relatively later arrival times that could not be fixed by adding a 3rd layer to the model.

For the liquid phantoms, the DT modeling was not making any sense. Considerable effort was spent on characterizing the lid made of PLA, to no avail. There is a well known way to quantify optical properties in media using semi-infinite (SI) and infinite medium (IM)

models based on DT and DTOF moments [35]. In particular, these methods are effective for estimation $\mu_s{}'$ [19] and thus gave us an avenue for exploration despite the layered DT model setbacks. Using the moments subtraction method described in section 1.3, reasonable estimates of $\mu_s{}'$ can be made in phantoms with high scattering and uniform $\mu_s{}'$.

Both the liquid and solid phantoms had nonideal design features. in particular, the errors in DT fitting for the liquid phantom with both three layer and two layer models showed that there might be something amiss at the boundary between the two layers. As thickness of the surface layer increased, the amount of error at later arrival times increased. This may have been due to a leak in the container that produced an air bubble that grew over time. It is important to control for these potential sources of error, to see if they were the cause and also to discover the limitations of the DT model.

With the solid phantom measurements, one source of error in the model could have come from the 1 cm slab on the top layer having a much lower expected scattering coefficient. The ideal solid phantom would have had high scattering in both the top and the bottom layers. DT is known to cause errors when modeling thin layers with low scattering, such as the cerebral spinal fluid layer in a human head [58]. Similarly for the liquid phantoms, the PLA separating the top and the bottom was very thin with very low scatter.

Achieved objectives and significance

The specific goal of all of this work was to find the sources of error for layered DT and time-gated TRDRS that arose in both solid and liquid phantom studies. It was observed that the measured DTOF clearly shifted in response to changes of top layer thickness whereas the ungated signals did not respond. This is a remarkable result that would seem to show that time-gating can indeed be used to make characterization of layered media possible at a larger depth. However, unexplained errors between these measurements and layered DT showed limited practicality for resolving the optical properties of each layer accurately.

Hypothetically, the errors came from two possible sources: (1) the sample design or (2) the light propagation model itself. If we could prove the error was coming from design flaws of the liquid phantoms, such as from an air bubble or from the 850 μm thin PLA lid, then we would just need to redesign the phantom and take note of the features that cannot be modeled (bubbles and thin plastic layers). If the model itself was the main culprit, we would need to use other analytical methods or models to quantify chromophore concentrations of deeper layers [10].

Achieving this objective of pinpointing error sources would show whether researchers

whose aim is to probe deeper using time-gated TRDRS should pursue layered DT analysis or avoid it. The objective was partially achieved by showing that adding an additional layer for the thin PLA lid to our DT model had negligible impact on the error. This showed us that the DT model cannot account for the thin layer and that using a phantom of such a design is certainly not practical to resolve the deeper optical properties in the layered sample. It was also shown previously that the phantom made of two solid slab layers had lower overall error, which may mean that the layered DT can be useful, but only when the interface between the two layers is many times thinner than the PLA lid (as is the case for two solid slabs separated by a very thin gap of air). These results indicate that the error is tied to both the phantom design and the model. This leads us to the question of whether designing phantoms more like the solid phantom can avoid the errors consistently? Furthermore, can these more ideal solid phantoms tell us how well time-gated TRDRS can perform on real tissues?

Future work

Further research is needed to fully answer whether errors can be sufficiently reduced through phantom design. More solid slab layered phantoms need to be made with calibrated optical properties and measured using gated and ungated TRDRS. Solid slab phantoms can be made using mixtures of bovine hemoglobin powder and intralipid mixed with gelatin [59]. If these measurements show reduced error, it would prove that the errors were a result of the liquid phantom design and the errors can be reduced through using solid slabs.

Another experiment with a similar objective is to use liquid phantoms again, but to control for possible air bubble formation. This could be done by 3D printing a container where the PLA lid is sealed to the bottom chamber (see Figure 3.3). That way, once the bottom chamber is filled with no air bubbles, it stays that way because there is no longer a crease between the lid and the bottom chamber, where the slow leaking occurred during liquid phantom experiments. If this shows that errors can be significantly reduced, again the the design of the phantom can solve the problem and we would also be able to use liquid phantoms.

Acronyms

ADC analog-to-digital converter. 21

AOTF acousto-optic tunable bandpass filter. 11

APD avalanche photodiode. 14

AQC active quenching circuit. 17

CCD charge coupled device. 19

CFD constant fraction discriminator. 21

CU control unit. 26

CWDRS continuous-wave diffuse reflectance spectroscopy. 2

DCR dark count rate. 16

DOS diffuse optical spectroscopy. 1, 3

DT diffusion theory. 6, 7, 10, 32, 56

DTOF distribution of time-of-flight. 8, 9, 41, 56

ECL emitter-coupled logic. 22

FFT fast Fourier transform. 38

FGSPAD FastGatedSPAD. 27

IAD inverse adding-doubling algorithm. 39, 43

IM infinite medium. 9, 10, 56

IRF instrument response function. 8, 9

LM Levenberg-Marquardt. 46

NIR near-infrared. 1

OCT optical coherence tomography. 37

PDMS polydimethylsiloxane. 32

PLA polylactic acid. 34, 35, 56, 57

PMT photomultiplier tubes. 11

PQC passive quenching circuit. 16, 18

PUR polyurethane. 32

RTE radiative transfer equation. 1, 5, 32

SC supercontinuum. 13

SDS source-detector separation. 2, 4, 9, 10, 32

SI semi-infinite. 7, 9, 56

SPAD single-photon avalanche photodiodes. 11

SPAD single-photon avalanche photodiode. 14, 15

TAC time-to-analog converter. 21

TCSPC time-correlated single photon counting. 19

TPSF temporal point spread function. 8, 9, 33

TRDRS time-resolved diffuse reflectance spectroscopy. 2, 3, 32, 41, 56

Bibliography

[1] Akira Ishimaru. *Wave Propagation and Scattering in Random Media: Single Scattering and Transport Theory, Volume 1.* Academic Press, California, 1978.

[2] T. Durduran, R. Choe, W. B. Baker, and A. G. Yodh. Diffuse optics for tissue monitoring and tomography. *Reports on Progress in Physics*, 73(7):076701, 2010.

[3] Robert H. Wilson, Karthik Vishwanath, and Mary Ann Mycek. Optical methods for quantitative and label-free sensing in living human tissues: principles, techniques, and applications. *Advances in Physics: X*, 1(4):523–543, 2016.

[4] Marco Ferrari and Valentina Quaresima. A brief review on the history of human functional near-infrared spectroscopy (fNIRS) development and fields of application. *NeuroImage*, 63(2):921–935, 2012.

[5] Adelina Pellicer and María del Carmen Bravo. Near-infrared spectroscopy: A methodology-focused review. *Seminars in Fetal and Neonatal Medicine*, 16(1):42–49, 2011.

[6] A. P. Gibson, J. C. Hebden, and S. R. Arridge. Recent advances in diffuse optical imaging. *Physics in Medicine and Biology*, 50(4):R1–R43, 2005.

[7] Farizio Martelli, Samuele Del Bianco, Andrea Ismaelli, and Giovanni Zaccanti. *Light Propagation through Biological Tissue and Other Diffusive Media: Theory, Solutions and Software.* SPIE Press, Bellingham, Washington, 2009.

[8] Steven L. Jacques and Brian W. Pogue. Tutorial on diffuse light transport. *Journal of Biomedical Optics*, 13(4):041302, 2008.

[9] George Alexandrakis, Thomas J Farrell, and Michael S Patterson. Accuracy of the diffusion approximation in determining the optical properties of a two-layer turbid medium. *Applied Optics*, 37(31):7401–7409, 1998.

[10] Daniel Milej, Androu Abdalmalak, Ajay Rajaram, Amandeep Jhajj, Adrian M. Owen, and Keith St. Lawrence. Incorporating early and late-arriving photons to improve the reconstruction of cerebral hemodynamic responses acquired by time-resolved near-infrared spectroscopy. *Journal of Biomedical Optics*, 26(5):056003, 5 2021.

[11] Felix Scholkmann, Stefan Kleiser, Andreas Jaakko Metz, Raphael Zimmermann, Juan Mata Pavia, Ursula Wolf, and Martin Wolf. A review on continuous wave functional near-infrared spectroscopy and imaging instrumentation and methodology. *NeuroImage*, 85:6–27, 2014.

[12] Aleh Sudakou, Frédéric Lange, Helene Isler, Pranav Lanka, Stanislaw Wojtkiewicz, Piotr Sawosz, Daniel Ostojic, Martin Wolf, Antonio Pifferi, Ilias Tachtsidis, Adam Liebert, and Anna Gerega. Time-domain NIRS system based on supercontinuum light source and multi-wavelength detection: validation for tissue oxygenation studies. *Biomedical Optics Express*, 12(10):6629–6650, 2021.

[13] Sanathana Konugolu Venkata Sekar, Pranav Lanka, Andrea Farina, Alberto Dalla Mora, Stefan Andersson-Engels, Paola Taroni, and Antonio Pifferi. Broadband time domain diffuse optical reflectance Spectroscopy: A review of systems, methods, and applications. *Applied Sciences (Switzerland)*, 9(24):5465, 2019.

[14] Yukio Yamada, Hiroaki Suzuki, and Yutaka Yamashita. Time-domain near-infrared spectroscopy and imaging: A review. *Applied Sciences (Switzerland)*, 9(6):1127, 2019.

[15] Piotr Sawosz and Adam Liebert. Method to improve the depth sensitivity of diffuse reflectance measurements to absorption changes in optically turbid medium. *Biomedical Optics Express*, 10(10):5031–5041, 2019.

[16] Lucia Zucchelli, Davide Contini, Rebecca Re, Alessandro Torricelli, and Lorenzo Spinelli. Method for the discrimination of superficial and deep absorption variations by time domain fNIRS. *Biomedical Optics Express*, 4(12):2893, 2013.

[17] Juliette Selb, Danny K. Joseph, and David A. Boas. Time-gated optical system for depth-resolved functional brain imaging. *Journal of Biomedical Optics*, 11(4):044008, 2006.

[18] Michael Helton, Mary-Ann Mycek, and Karthik Vishwanath. Direct estimation of the reduced scattering coefficient from experimentally measured time-resolved reflectance via Monte Carlo based lookup tables. *Biomedical Optics Express*, 11(8):4366, 2020.

[19] Daniel Milej, Androu Abdalmalak, Dariusz Janusek, Mamadou Diop, Adam Liebert, and Keith St. Lawrence. Time-resolved subtraction method for measuring optical properties of turbid media. *Applied Optics*, 55(7):1507–1513, 2016.

[20] Antonio Pifferi, Davide Contini, Alberto Dalla Mora, Andrea Farina, Lorenzo Spinelli, and Alessandro Torricelli. New frontiers in time-domain diffuse optics, a review. *Journal of Biomedical Optics*, 21(9):091310, 2016.

[21] Alberto Tosi, Alberto Dalla Mora, Franco Zappa, Angelo Gulinatti, Davide Contini, Antonio Pifferi, Lorenzo Spinelli, Alessandro Torricelli, and Rinaldo Cubeddu. Fast-gated single-photon counting technique widens dynamic range and speeds up acquisition time in time-resolved measurements. *Optics Express*, 19(11):10735–10746, 5 2011.

[22] Alberto Dalla Mora, Alberto Tosi, Franco Zappa, Sergio Cova, Davide Contini, Antonio Pifferi, Lorenzo Spinelli, Alessandro Torricelli, and Rinaldo Cubeddu. Fast-gated single-photon avalanche diode for wide dynamic range near infrared spectroscopy. *IEEE Journal on Selected Topics in Quantum Electronics*, 16(4):1023–1030, 2010.

[23] Antonio Pifferi, Alessandro Torricelli, Lorenzo Spinelli, Davide Contini, Rinaldo Cubeddu, Fabrizio Martelli, Giovanni Zaccanti, Alberto Tosi, Alberto Dalla Mora, Franco Zappa, and Sergio Cova. Time-resolved diffuse reflectance using small source-detector separation and fast single-photon gating. *Physical Review Letters*, 100(13):1–4, 2008.

[24] Roberts Leibuss, Arnija Reihmane, Lāsma Baltace, Kārlis Baltacis, Sabīne Štelmahere, Vineta Zemīte, Yuri Dekhtyar, and Pēteris Stradiņš. Cerebral Oximetry Measurements Results Depending on a Preclinical Skull Phantom Model. In *Proceedings of the Latvian Academy of Sciences. Section B. Natural, Exact, and Applied Sciences.*, volume 75, pages 371–378, 2021.

[25] Freija Geldof, Behdad Dashtbozorg, Benno H W Hendriks, Henricus J C M Sterenborg, and Theo J M Ruers. Layer thickness prediction and tissue classification in two-layered tissue structures using diffuse reflectance spectroscopy. *Scientific Reports*, 12(1698):05751, 2022.

[26] Pavitra S. Rudraiah, Hamootal Duadi, and Dror Fixler. Bottom layer absorption coefficients extraction from two-layer phantoms based on crossover point in diffuse reflectance. *Journal of Biomedical Optics*, 26(11):1–11, 2021.

[27] Lin Yang, Heidrun Wabnitz, Thomas Gladytz, Aleh Sudakou, Rainer Macdonald, and Dirk Grosenick. Space-enhanced time-domain diffuse optics for determination of tissue optical properties in two-layered structures. *Biomedical Optics Express*, 11(11):6570, 2020.

[28] S R Arridge, M Cope, and D T Delpy. The theoretical basis for the determination of optical pathlengths in tissue: temporal and frequency analysis. *Physics in Medicine and Biology*, 37(7):1531–1560, 7 1992.

[29] Alwin Kienle and Michael S. Patterson. Improved solutions of the steady-state and the time-resolved diffusion equations for reflectance from a semi-infinite turbid medium. *Journal of the Optical Society of America A*, 14(1):246–254, 1997.

[30] Michael S Patterson, B Chance, and B C Wilson. Time resolved reflectance and transmittance for the non-invasive measurement of tissue optical properties. *Applied Optics*, 28(12):2331–2336, 1989.

[31] Daniele Contini, Fabrizio Martelli, and Giovanni Zaccanti. Photon migration through a turbid slab described by a model based on diffusion approximation I Theory. *Applied Optics*, 36(19):4587, 1997.

[32] André Liemert and Alwin Kienle. Light diffusion in a turbid cylinder II. Layered case. *Optics Express*, 18(9):9266, 2010.

[33] André Liemert and Alwin Kienle. Application of the Laplace transform in time-domain optical spectroscopy and imaging. *Journal of Biomedical Optics*, 20(11):110502, 2015.

[34] J A C Weideman and L N Trefethen. Parabolic and hyperbolic contours for computing the Bromwich integral. *Mathematics of Computation*, 76(259):1341–1356, 2007.

[35] Adam Liebert, Heidrun Wabnitz, Dirk Grosenick, Michael Möller, Rainer Macdonald, and Herbert Rinneberg. Evaluation of optical properties of highly scattering media by moments of distributions of times of flight of photons. *Applied Optics*, 42(28):5785, 2003.

[36] Alberto Dalla Mora, Laura Di Sieno, Rebecca Re, Antonio Pifferi, and Davide Contini. Time-Gated Single-Photon Detection in Time-Domain Diffuse Optics: A Review. *Applied Sciences*, 10:1101, 2020.

[37] Alessandro Torricelli, Davide Contini, Antonio Pifferi, Matteo Caffini, Rebecca Re, Lucia Zucchelli, and Lorenzo Spinelli. Time domain functional NIRS imaging for human brain mapping. *NeuroImage*, 85:28–50, 2014.

[38] Frédéric Lange, Luca Giannoni, and Ilias Tachtsidis. The use of supercontinuum laser sources in biomedical diffuse optics: Unlocking the power of multispectral imaging. *Applied Sciences (Switzerland)*, 11(10):4616, 2021.

[39] [https://www.rp-photonics.com/supercontinuum_generation.html article on 'Supercontinuum Generation' in the RP Photonics Encyclopedia], 6 2022.

[40] S. Cova, M. Ghioni, A. Lacaita, C. Samori, and F. Zappa. Avalanche photodiodes and quenching circuits for single-photon detection. *Applied Optics*, 35(12):1956–1976, 1996.

[41] Wolfgang Becker. Time-Correlated Single Photon Counting (TCSPC). In *Advanced time-correlated single photon counting techniques*, chapter 2, pages 20–24. Springer, Berlin, Germany, 2005.

[42] Wolfgang Becker. Time Measurement Block. In *Advanced time-correlated single photon counting techniques*, chapter 4, pages 50–57. Springer, Berlin, Germany, 2005.

[43] Wolfgang Becker. Setting the TCSPC System Parameters. In *Advanced time-correlated single photon counting techniques*, chapter 7, pages 317–330. Springer, Berlin, Germany, 2005.

[44] W. Becker. *Advanced time-correlated single photon counting techniques*. Springer-Verlag Berlin Heidelberg, 2005.

[45] Micro Photon Devices SRL. FastGatedSPAD. `http://www.micro-photon-devices.com/Products/SPAD-by-Wavelength/400nm-900nm/FastGATED-SPAD`. Accessed: 2022-06-02.

[46] Davide Contini, Alberto Dalla Mora, Lorenzo Spinelli, Andrea Farina, Alessandro Torricelli, Rinaldo Cubeddu, Fabrizio Martelli, Giovanni Zaccanti, Alberto Tosi, Gianluca Boso, Franco Zappa, and Antonio Pifferi. Effects of time-gated detection in diffuse optical imaging at short source-detector separation. *Journal of Physics D: Applied Physics*, 48(4):045401, 2015.

[47] Ben Aernouts, Robbe Van Beers, Rodrigo Watté, Jeroen Lammertyn, and Wouter Saeys. Dependent scattering in Intralipid® phantoms in the 600-1850 nm range. *Optics Express*, 22(5):6086, 2014.

[48] Lorenzo Spinelli, Fabrizio Martelli, Andrea Farina, Antonio Pifferi, Alessandro Torricelli, Rinaldo Cubeddu, and Giovanni Zaccanti. Calibration of scattering and absorption properties of a liquid diffusive medium at NIR wavelengths. Time-resolved method. *Optics Express*, 15(11):6589, 2007.

[49] Rene Michels, Florian Foschum, and Alwin Kienle. Optical properties of fat emulsions. *Optics Express*, 16(8):5907, 2008.

[50] L. Spinelli, M. Botwicz, N. Zolek, M. Kacprzak, D. Milej, P. Sawosz, A. Liebert, U. Weigel, T. Durduran, F. Foschum, A. Kienle, F. Baribeau, S. Leclair, J.-P. Bouchard, I. Noiseux, P. Gallant, O. Mermut, A. Farina, A. Pifferi, A. Torricelli, R. Cubeddu, H.-C. Ho, M. Mazurenka, H. Wabnitz, K. Klauenberg, O. Bodnar, C. Elster, M. Bénazech-Lavoué, Y. Bérubé-Lauzière, F. Lesage, D. Khoptyar, A. A. Subash, S. Andersson-Engels, P. Di Ninni, F. Martelli, and G. Zaccanti. Determination of reference values for optical properties of liquid phantoms based on Intralipid and India ink. *Biomedical Optics Express*, 5(7):2037–2053, 2014.

[51] Vinoin Devpaul Vincely and Karthik Vishwanath. Accuracy of retrieving optical properties from liquid tissue phantoms using a single integrating sphere. *Applied Optics*, 61(2):375–385, 2022.

[52] Weihao Chen, Georgios Tsissios, Anthony Sallese, Byran Smucker, Anh Thu Nguyen, Junfan Chen, Hui Wang, and Katia Del Rio-Tsonis. In vivo imaging of newt lens regeneration: Novel insights into the regeneration process. *Translational Vision Science and Technology*, 10(10):1–12, 2021.

[53] Judy Zouaoui, Laura Di Sieno, Lionel Hervé, Antonio Pifferi, Andrea Farina, Alberto Dalla Mora, Jacques Derouard, and Jean-Marc Dinten. Quantification in time-domain diffuse optical tomography using Mellin-Laplace transforms. *Biomedical Optics Express*, 7(10):4346–4363, 2016.

[54] S. Del Bianco, F. Martelli, F. Cignini, G. Zaccanti, A. Pifferi, A. Torricelli, A. Bassi, P. Taroni, and R. Cubeddu. Liquid phantom for investigating light propagation through layered diffusive media. *Optics Express*, 12(10):2102–2111, 2004.

[55] Michael C. Helton, Carter McMaster, Mary-Ann Mycek, and Karthik Vishwanath. Calibration free, time-resolved diffuse optical spectroscopy using combined Monte-Carlo and diffusion theory. In Adam Wax and Vadim Backman, editors, *Proceedings of the SPIE*, page 116570. SPIE, 2021.

[56] Michael Helton, Mary-Ann Mycek, and Karthik Vishwanath. Reconstruction of optical coefficients in turbid media using time-resolved reflectance and calibration-free instrument response functions. *Biomedical Optics Express*, 13(3):1595–1608, 3 2022.

[57] Rinaldo Cubeddu, Antonio Pifferi, Paola Taroni, Alessandro Torricelli, and Gianluca Valentini. Experimental test of theoretical models for time-resolved reflectance. *Medical Physics*, 23(9):1625–1633, 1996.

[58] Anna Custo, William M. Wells, Alex H. Barnett, Elizabeth M.C. Hillman, and David A. Boas. Effective scattering coefficient of the cerebral spinal fluid in adult head models for diffuse optical imaging. *Applied Optics*, 45(19):4747–4755, 2006.

[59] Hanna Jonasson, Chris D. Anderson, and Rolf B. Saager. Water and hemoglobin modulated gelatin-based phantoms to spectrally mimic inflamed tissue in the validation of biomedical techniques and the modeling of microdialysis data. *Journal of Biomedical Optics*, 27(07):1–11, 2022.